Journal of Computational Physics **171,** 1–46 (2001)
doi:10.1006/jcph.2001.6761, available online at http://www.idealibrary.com on IDEAL®

A Curvilinear Version of the Bryan–Cox–Semtner Ocean Model and Its Representation of the Arctic Circulation

Ross J. Murray* and C. J. C. Reason*,†

*School of Earth Sciences, University of Melbourne, Melbourne, Australia; and †EGS and Oceanography Departments, University of Cape Town, South Africa
E-mail: rjmury@earthsci.unimelb.edu.au, cjr@egs.uct.ac.za

Received June 22, 1999; revised March 1, 2001

Continuous and finite difference forms of the governing equations are derived for a version of the Bryan–Cox–Semtner ocean general circulation model which has been recast in orthogonal, transversely curvilinear coordinates. The coding closely follows the style of the Geophysical Fluid Dynamics Laboratory modular ocean model No. 1. Curvilinear forms are given for the tracer, internal momentum, and stream function calculations, with the options of horizontal and isopycnal diffusion, eddy-induced transport, nonlinear viscosity, and semiimplicit treatment of the Coriolis force. The model is designed to operate on a rectangular three-dimensional array of points and can accommodate reentrant boundary conditions at both 'northern' and 'east–west' boundaries. Horizontal grid locations are taken as input and need to be supplied by a separate grid generation program. The advantages of using a better behaved and more economical grid in the north polar region are investigated by comparing simulations performed on two curvilinear grids with one performed on a latitude–longitude grid and by comparing filtered and unfiltered latitude–longitude simulations. Resolution of horizontally separated currents in Fram Strait emerges as a key challenge for representing exchanges with the Arctic in global models.

Key Words: ocean modelling; curvilinear grids; Arctic Ocean.

1. INTRODUCTION

The convergence of meridians at the North Pole in latitude–longitude models creates two major computational problems for simulations in which the Arctic is included. The first is that of integrating the prognostic equations at the polar point. The difficulty is normally obviated by including a row of land points at the northern array boundary; however, this creates a small 'polar island,' which, even when reduced to a single velocity point, obstructs the transpolar flow and distorts the tracer fields. These defects may be quite important in

0021-9991/01 $35.00

models with coupled sea-ice and time-varying surface flux forcings. Although currents in the Arctic Ocean are sluggish, they have the potential to affect other parts of the world ocean through the export of sea ice and the water mass transformations that occur in the Greenland Sea. We have found [40] that the need for a polar island and the distortion it produces can be avoided quite satisfactorily by treating the polar grid row as a single composite prognostic tracer point, as has also been done in the ocean component of the NCAR climate model [42].

The second problem is the severe limitation on computational time steps imposed by the small zonal grid spacings that occur near the pole. This is usually dealt with by truncating or selectively damping the shorter zonal wavelengths, which most limit the time step, although other methods have recently been proposed for ocean applications, namely variable time stepping [60] and using a reduced grid [64]. Fourier filtering is the method most commonly employed to avoid the time step restriction in ocean models, but this can be an expensive remedy and one which tends to produce spurious features in the solution. These can be the result of Gibbs phenomena or the separate filtering of variables and may take the forms of static instabilities, noisy vertical velocities, and small perturbations in the horizontal velocities [40].

While both the problems discussed above have 'fixes,' a highly convergent grid with large cell aspect ratios and rapid cell size variation is not ideal for numerical modelling. Aside from the impact that these properties may have on truncation errors, such a grid is computationally inefficient and represents topographic and ocean features poorly. Reducing the meridional grid spacing in step with the zonal spacing, as on a Mercator grid, can (up to some latitude at which it must be stopped) reduce cell distortion, but only at the cost of creating a time step limitation in the meridional direction and compounding the grid inefficiency.

The problems and costs of grid convergence can be circumvented altogether by designing a grid that places the poles outside the ocean domain. Because suitable land antipodes for them do not exist [38], a simple rotation of the conventional spherical grid does not offer any advantage for modelling the global ocean. One solution, proposed by Deleersnijder *et al.* [15] and Eby and Holloway [17], is to use a *composite-rotated* grid, consisting of a 90°-rotated grid in the North Atlantic and Arctic Oceans joined at the equator in the Atlantic to a conventional grid, which is used for the rest of the world ocean. This grid is of very particular construction and suffers from a discontinuity in grid spacing at the join, which has been recognized as a potential source of truncation errors at the equator. Tests carried out by Eby and Holloway [17] and Coward *et al.* [11] have indicated that the effects of the coupling on the ocean solution and equatorial wave propagation would be small and tolerable, and the two-grid scheme has been implemented in the ocean circulation and climate modelling (OCCAM) project high resolution model [63]. However, the grid also suffers from a possibly inadequate resolution in the Arctic when used in coarse resolution simulations and from an incompatibility of subgrids at the Bering Strait.

A more general and flexible approach, and one which avoids these defects and limitations, is the use of an orthogonal curvilinear grid. Several techniques are now available for generating orthogonal grids with global continuity. A number of diverse methods have been proposed for constructing global orthogonal grids by analytical and semianalytical techniques about prescribed singular points by Murray [38]. Two meshes of semianalytical construction have also been developed by other groups. One of these has recently been described by Madec and Imbard [34] and is being used by the Laboratoire d'Océanographie

Dynamique et de Climatology (LODYC) (*vide* Marti *et al.* [36]); the other has been constructed upon similar lines by Smith *et al.* [57] and is being used in the parallel ocean program model. Each consists of a conventional southern hemisphere grid joined smoothly to a distorted northern hemisphere grid with an off-axis pole and in such a way as to overcome the shortcomings of the composite–rotated grid.

Curvilinear coordinates have already been used in some regional ocean models: in the semispectral primitive equation model (SPEM) of Haidvogel *et al.* [27], and in a curvilinear version [37] of the coastal ocean numerical model of Blumberg and Mellor [5]. The grids required for both models are generated by a program in which the conformal boundary fitting grid generation techniques of Ives and Zacharias [30] have been adapted for ocean model grids by Wilkin [65] and Wilkin and Hedström [66]. Examples of meshes generated by this program have been illustrated by Häkkinen and Mellor [28] and Ezer and Mellor [18]. In the applications for which the method was designed, the purpose of using curvilinear grids has been to allow the bounding coordinates to follow coastlines, rather than to displace polar singularities.

Boundary fitting methods have not yet been brought to the point of being able to create global grids with matched reentrant boundaries; but this is a problem of grid generation, not numerical modelling. There would be nothing to prevent one of the global grids mentioned previously from being used in one of the regional models. These models contain some attractive features, such as the use of terrain-following vertical coordinates, the implementation of advanced mixing schemes, and (in later versions) a free surface treatment. Because they were designed principally to handle regional scale dynamics, they may not necessarily be the most appropriate for global integrations. Both are discretised on an Arakawa C grid, which gives a more accurate representation of the geostrophic adjustment when the Rossby radius is resolved (e.g., [8, 61]), as it often is in regional models. For coarse resolution global models, the B grid gives the better adjustment and allows a more exact solution when the Coriolis term is treated semiimplicitly [6]. The stability condition on an explicit Coriolis term is more likely to be a limiting factor in coarse resolution models than in fine resolution models, where the momentum time step must be very much smaller than $1/f$.

The oldest and most familiar ocean model, and the one still most commonly used in global modelling applications, is the one that developed from the work of Bryan and Cox in the 1960s, with contributions by Semtner in the 1970s [6, 9, 12, 52]. Its principal defining features are the use of an Arakawa B grid, constant depth levels, a rigid lid condition, a no-slip lateral boundary condition, centred advection, and leap-frog time stepping. In recent years, the model has been coded for efficient vectorisation and option selection in the modular ocean model format at the Geophysical Fluid Dynamics Laboratory (GFDL), Princeton, New Jersey [43–45]. In its modular format, the model has acquired and is still acquiring a range of physical parameterisations and numerical processing options, but in its characteristic features it remains broadly unchanged. Orthogonal curvilinear coordinates have now been implemented or are being implemented in the model by other groups, e.g., by Smith *et al.* [57]; however, when we first contemplated doing this, the model was not available in this form, and it was felt that, in view of its utility for global climate modelling, a version should be written in orthogonal curvilinear coordinates, but incorporating the same numerics, the same basic physical parameterisations, and the same 'modular' programming style as the GFDL model. One of the purposes of this paper is to describe the resulting model. The base code that we used for this conversion was the modular ocean model, version 1 (MOM1); however, it is not the coding details, but rather the algebraic statement

of the numerics that is presented here, and this would also be relevant to the conversion of other spherical model codes derived from it.

The prognostic equations and the continuity equation involve vector differential operators. The forms of these in curvilinear coordinates differ from their spherical counterparts, and the task has been to rewrite the governing equations in terms of these operators. Continuous forms of the governing equations are derived from the curvilinear forms of the differential operators in Section 2. The finite difference forms derived from these are given in Section 3. Supplementary details of the model and a brief treatment of its energetic consistency is given in the appendices. The conversion has been limited to the case of orthogonal curvilinearity in the horizontal and with constant levels in the vertical; the further generalisation to a horizontally variable vertical discretisation, such as has been implemented in the spherical model by Gerdes [21] and, more narrowly, in sigma and isopycnal coordinate models, has not been attempted at this stage.

The advantages of using orthogonal curvilinear grids in an ocean model derive from three properties they possess: (1) their ability to follow coastlines and avoid the need to carry out wasteful computations at land points; (2) their ability to remove the north grid-pole from the ocean domain and place singularities over land in such a way as to minimise convergence problems; and (3) their ability to provide grid size variation beyond that available from grid convergence and coordinate rescaling and, hence, a global grid with a high density of grid points in a focal region and lower density elsewhere. The first of these has already been exploited in regional models, as mentioned above, and the third has been investigated by Murray and Reason [41] using a global grid designed to focus resolution in the Indian Ocean sector. The model experiments reported in Section 4 focus on the second advantage, that of using curvilinear grids for removing the north grid pole from the ocean domain and, more particularly, the advantages of doing this for representing the Arctic Ocean in global models. This was investigated by comparing simulations of the North Atlantic and Arctic Oceans using one latitude–longitude grid and two curvilinear grids.

2. ORTHOGONAL CURVILINEAR FORM OF THE PRIMITIVE EQUATIONS

2.1. *Curvilinear Forms of the Differential Operators*

The primitive equations for an ocean obeying the hydrostatic, incompressible, and Boussinesq assumptions may be given as

$$\frac{\partial \mathbf{u}_{\mathrm{H}}}{\partial t} = -(\mathbf{u}\cdot\boldsymbol{\nabla}\mathbf{u})_{\mathrm{H}} - f\mathbf{k}\times\mathbf{u} - \frac{1}{\rho}\boldsymbol{\nabla}_{\mathrm{H}}p + (\boldsymbol{\nabla}\cdot\mathsf{T})_{\mathrm{H}} + (\mathbf{Q}_{\mathbf{u}})_{\mathrm{H}}, \tag{1}$$

$$\frac{\partial T}{\partial t} = -\mathbf{u}\cdot\boldsymbol{\nabla}T + \boldsymbol{\nabla}\cdot(\mathsf{K}\boldsymbol{\nabla}T) + Q_T, \tag{2}$$

$$\frac{\partial S}{\partial t} = -\mathbf{u}\cdot\boldsymbol{\nabla}S + \boldsymbol{\nabla}\cdot(\mathsf{K}\boldsymbol{\nabla}S) + Q_S, \tag{3}$$

$$\boldsymbol{\nabla}\cdot\mathbf{u} = 0, \tag{4}$$

$$-\frac{1}{\rho}\frac{\partial p}{\partial z} = g, \tag{5}$$

$$\rho = \rho(T, S, p) \approx \rho(T, S, z), \tag{6}$$

where $\mathbf{u}$ is the velocity, T is the temperature, S is the salinity, $f = 2\Omega \sin\phi$ is the Coriolis factor, ρ is the density, T is the viscous shear stress tensor, K is the diffusivity tensor, g is the gravitational constant, $(\mathbf{Q_u})_{\mathrm{H}}$, Q_T, and Q_S are source terms, and the horizontal part of a vector quantity is denoted by the subscript 'H.' Eqs. (1)–(5) include vector differential operators, whose form depends on the properties of the coordinate system adopted.

The curvilinear system is described by the two horizontal and one vertical nondimensional grid variables $(\xi_1, \xi_2, \xi_3) \equiv (\xi, \eta, \zeta)$ and the metric coefficients or factors $h_1 = \partial x/\partial\xi_1$, $h_2 = \partial y/\partial\xi_2$, and $h_3 = \partial z/\partial\xi_3$, where (x, y, z) are arbitrarily referenced distances measured along the grid contours. The local directions of the ξ_1, ξ_2, and ξ_3 axes define the unit base vectors $(\hat{\mathbf{e}}_1, \hat{\mathbf{e}}_2, \hat{\mathbf{e}}_3)$. The horizontal velocity components $(u_1, u_2) \equiv (u, v)$ are resolved parallel to the corresponding base vectors. By convention, the positive ξ_1 and ξ_2 axes are taken to be the ones most nearly aligned with the east and north directions over most of the grid, and the contours that they follow are referred to as 'grid meridians' and 'grid parallels.' In the special case of a latitude–longitude grid, the metric factors are

$$h_1 = a\delta\lambda\cos\phi, \qquad h_2 = a\delta\phi,$$

where a is the radius of the Earth. For consistency with the horizontal terms, the vertical terms are also rendered in terms of grid variables and spacings, although the latter are constant in the horizontal. The vertical coordinates ξ_3 and z, and the vertical velocity $u_3 = w$, are taken to be positive in the upward direction in the differential and finite difference equations.

General orthogonal curvilinear forms of the vector differential operators are given in Malvern ([35] Appendix II) and other standard texts. The transverse curvilinear forms used in this paper are given in Appendix A.

2.2. *Time Integration*

The time marching procedure is exactly the same as in the GFDL model; however, the method will be reiterated in order to introduce the major terms, whose curvilinear forms are different.

Stability and second order accuracy in time are achieved by the use of a leapfrog scheme, in which prognostic variables are integrated over a double time interval $(2\delta t)$, i.e., from time level $(n-1)$ to time level $(n+1)$. Terms in the prognostic equations are normally centred in time, except for the diffusive and viscous terms, which require a forward rather than a centred time difference for stability [50]. To avoid decoupling of the solutions at adjacent time steps, a forward or similar integration over a single time interval is substituted at occasional time steps.

The prognostic equation for tracer $T_s (T_1 = T, T_2 = S)$ may be written

$$\frac{T_s^{(n+1)} - T_s^{(n-1)}}{2\delta t_{\mathrm{ts}}} = G_{T_s},$$

where δt_{ts} is the tracer time step, which may differ from the momentum time step, δt_{uv}, and may vary from one level to another [7], and

$$G_{T_s} = -\mathbf{u}\cdot\boldsymbol{\nabla}T_s^{(n)} + \boldsymbol{\nabla}\cdot\left(\mathsf{K}\boldsymbol{\nabla}T_s^{(n-1)}\right) + Q_{T_s}^{(n)}$$

combines all the known forcings. When the vertical component of the diffusivity tensor, K_{33}, is enhanced by tensor rotation or stability-dependent vertical mixing, the time step

limit for diffusion, $\delta t_{\rm ts} \le h_3^2/(4K_{33})$, may be exceeded, and the mixing term will require an implicit solution of

$$\frac{T_s^{(n+1)} - T_s^{(n-1)}}{2\delta t_{\rm ts}} = G_{T_s} + \alpha_{\rm vdiff}\frac{\partial}{\partial z}\left[K_{33}\frac{\partial}{\partial z}\left(T_s^{(n+1)} - T_s^{(n-1)}\right)\right].$$

Solutions are stable at all time steps provided that $\frac{1}{2} \le \alpha_{\rm vdiff} \le 1$. The vertical mixing of horizontal momentum may be handled in the same way.

In the momentum equation, a rigid lid condition is imposed, which explicitly filters external gravity waves from the solution. The contribution to the pressure that would naturally arise from variation of the height of the free surface is replaced by a notional surface or rigid lid pressure, p_s. The total pressure at any point is the sum of p_s and a hydrostatic pressure, $\tilde{p}$, obtained by integrating Eq. (5); however, the surface pressure is not actually determined. Since p_s acts on all levels equally, it affects only the depth-averaged velocities (the external or barotropic mode) and has no effect on the depth-anomalous velocities (the internal or baroclinic mode). By solving the external and internal modes separately and taking the curl of the barotropic momentum equation, the surface pressure gradient term is eliminated. Because the depth-integrated flow is nondivergent, the resulting equation can be solved as an elliptical equation of the stream function tendency (see Section 2.9).

To overcome the restriction imposed by the need to resolve inertial oscillations, the Coriolis term may be calculated semiimplicitly; this is done by replacing the time-centred velocities in the explicit Coriolis term by a weighting α of their values at time $(n+1)$ and $(1-\alpha)$ of their values at $(n-1)$, viz.,

$$\frac{\mathbf{u}^{(n+1)} - \mathbf{u}^{(n-1)}}{2\delta t_{\rm uv}} = -f\mathbf{k}\times\left[\alpha\mathbf{u}^{(n+1)} + (1-\alpha)\mathbf{u}^{(n-1)}\right] + (\text{other forcings}).$$

Using the notation $\delta_{2t}\mathbf{u} = \mathbf{u}^{(n+1)} - \mathbf{u}^{(n-1)}$, the tendency term may be written

$$\frac{\delta_{2t}\mathbf{u}}{2\delta t_{\rm uv}} = -\alpha f\mathbf{k}\times\delta_{2t}\mathbf{u} - f\mathbf{k}\times\mathbf{u}^{(l)} + (\text{other forcings}),$$

where, to make the equation more general, the time level of the explicit part is defined as $l = n$ for explicit treatment ($\alpha = 0$) and $l = n-1$ for semiimplicit treatment ($\frac{1}{2} \le \alpha \le 1$). Transferring the time change part of the Coriolis term to the left-hand side (LHS) and combining the explicit part with the other known forcings, the momentum equation may now be written

$$\frac{\delta_{2t}\mathbf{u}}{2\delta t_{\rm uv}} + \alpha f\mathbf{k}\times\delta_{2t}\mathbf{u} = \mathbf{G_u} - \frac{1}{\rho_0}\boldsymbol{\nabla}_{\rm H}p_s^{(n)},$$

where

$$\mathbf{G_u} = -\mathbf{u}^{(n)}\cdot\boldsymbol{\nabla}\mathbf{u}^{(n)} - f\mathbf{k}\times\mathbf{u}^{(l)} - \frac{1}{\rho_0}\boldsymbol{\nabla}_{\rm H}\tilde{p}^{(n)} + \boldsymbol{\nabla}\cdot\mathsf{T}^{(n-1)} + \mathrm{Q}_{\mathbf{u}}^{(n)}$$

and is taken to include, in addition to the explicit forcings, any implicit vertical friction.

Because of the measures required to eliminate the surface pressure, the momentum equation, and hence the forcings, are divided into external and internal modes, viz.

$$\frac{\delta_{2t}\bar{\mathbf{u}}}{2\delta t_{\mathrm{uv}}} + \alpha f \mathbf{k} \times \delta_{2t}\bar{\mathbf{u}} = \overline{\mathbf{G}_{\mathbf{u}}} - \frac{1}{\rho_0}\boldsymbol{\nabla}_{\mathrm{H}} p_s^{(n)}, \tag{7}$$

$$\frac{\delta_{2t}\mathbf{u}'}{2\delta t_{\mathrm{uv}}} + \alpha f \mathbf{k} \times \delta_{2t}\mathbf{u}' = \mathbf{G}'_{\mathbf{u}}. \tag{8}$$

The time steps for the two modes are normally the same, but need not be. When the Coriolis term is semiimplicit, the internal mode is obtained by manipulation of Eq. (8) as

$$\frac{\delta_{2t}\mathbf{u}'}{2\delta t_{\mathrm{uv}}} = \left[\frac{\mathbf{G}_{\mathbf{u}} - (2\delta t_{\mathrm{uv}}\alpha f)\mathbf{k} \times \mathbf{G}_{\mathbf{u}}}{1 + (2\delta t_{\mathrm{uv}}\alpha f)^2}\right]',$$

the prime outside the bracket indicating the deviation from the vertical average. The external mode is obtained by combining the two terms on the LHS of Eq. (7) and solving the equation as described in Section 2.9.

2.3. *Continuity Equation*

Using Eq. (A4) from Appendix A, the continuity equation (Eq. 4) becomes

$$\boldsymbol{\nabla} \cdot \mathbf{u} = \frac{1}{h_1 h_2}\left[\frac{\partial(h_2 u_1)}{\partial \xi_1} + \frac{\partial(h_1 u_2)}{\partial \xi_2}\right] + \frac{1}{h_3}\frac{\partial u_3}{\partial \xi_3} = 0. \tag{9}$$

The vertical velocity, w, is calculated diagnostically by downward integration of the horizontal divergence,

$$u_3 = -\int_0^{\xi_3} \boldsymbol{\nabla}_{\mathrm{H}} \cdot \mathbf{u}\, h_3\, d\xi_3'.$$

2.4. *Advective Term for Tracers*

The continuity equation allows the advective terms in Eqs. (2) and (3) to be rephrased in flux form, which in the finite difference equations ensures conservation of the transported quantity. For the tracer T_s, substituting the flux $\mathbf{u}T_s$ for $\mathbf{V}$ in Eq. (A4) gives

$$-\mathbf{u} \cdot \boldsymbol{\nabla} T_s = -\boldsymbol{\nabla} \cdot (\mathbf{u} T_s) = -\frac{1}{h_1 h_2}\left[\frac{\partial(h_2 u_1 T_s)}{\partial \xi_1} + \frac{\partial(h_1 u_2 T_s)}{\partial \xi_2}\right] - \frac{1}{h_3}\frac{\partial(u_3 T_s)}{\partial \xi_3}. \tag{10}$$

2.5. *Diffusive Term for Tracers*

(*a*) *Horizontal mixing.* In many models, mixing is assumed to be transversely isotropic with respect to the vertical axis, with a horizontal diffusivity, A_H, being very much larger than the vertical diffusivity, K_H. The diffusivity tensor may be written

$$\mathsf{K} = \begin{bmatrix} A_H & 0 & 0 \\ 0 & A_H & 0 \\ 0 & 0 & K_H \end{bmatrix}.$$

Inserting this in Eq. (A5) yields

$$\boldsymbol{\nabla}\cdot(\mathsf{K}\boldsymbol{\nabla}T_s)=\frac{1}{h_1h_2}\left[\frac{\partial}{\partial\xi_1}\left(A_H\frac{h_2}{h_1}\frac{\partial T_s}{\partial\xi_1}\right)+\frac{\partial}{\partial\xi_2}\left(A_H\frac{h_1}{h_2}\frac{\partial T_s}{\partial\xi_2}\right)\right]+\frac{1}{h_3}\frac{\partial}{\partial\xi_3}\left(\frac{K_H}{h_3}\frac{\partial T_s}{\partial\xi_3}\right). \tag{11}$$

(*b*) *Isopycnal mixing.* Because tracers mix preferentially along isopycnal, not horizontal, surfaces, it is becoming common for modellers to use a rotated form of the mixing tensor, with a diffusivity A_I in the isopycnal direction. Following Cox [13], the form of the tensor originally proposed by Redi [49] is usually modified by the omission of certain components in the small angle approximation, the identification of diapycnal as vertical diffusivity (K_H), and the inclusion of a purely horizontal component of diffusivity (A_H) for numerical stability, then becoming

$$\mathsf{K}=\begin{bmatrix}A_I+A_H & 0 & A_IS_x\\ 0 & A_I+A_H & A_IS_y\\ A_IS_x & A_IS_y & A_I\left(S_x^2+S_y^2\right)+K_H\end{bmatrix}, \tag{12}$$

where

$$\mathbf{S}=\boldsymbol{\nabla}_\rho z=\left(\frac{-\rho_x}{\rho_z},\frac{-\rho_y}{\rho_z},0\right)$$

is the isopycnal slope vector and

$$(\rho_x,\rho_y,\rho_z)=\left(\frac{1}{h_1}\frac{\partial\rho}{\partial\xi_1},\frac{1}{h_2}\frac{\partial\rho}{\partial\xi_2},\frac{1}{h_3}\frac{\partial\rho}{\partial\xi_3}\right)$$

are the gradients of locally referenced potential density. The diffusion term then becomes

$$\begin{aligned}\boldsymbol{\nabla}\cdot(\mathsf{K}\boldsymbol{\nabla}T_s)=\frac{1}{h_1h_2}\Bigg\{&\frac{\partial}{\partial\xi_1}\left[h_2\left((A_I+A_H)\frac{1}{h_1}\frac{\partial T_s}{\partial\xi_1}+A_IS_x\frac{1}{h_3}\frac{\partial T_s}{\partial\xi_3}\right)\right]\\&+\frac{\partial}{\partial\xi_2}\left[h_1\left((A_I+A_H)\frac{1}{h_2}\frac{\partial T_s}{\partial\xi_2}+A_IS_y\frac{1}{h_3}\frac{\partial T_s}{\partial\xi_3}\right)\right]\Bigg\}\\&+\frac{1}{h_3}\frac{\partial}{\partial\xi_3}\Bigg\{A_I\left[S_x\frac{1}{h_1}\frac{\partial T_s}{\partial\xi_1}+S_y\frac{1}{h_2}\frac{\partial T_s}{\partial\xi_2}\right]\\&+\left[A_I\left(S_x^2+S_y^2\right)+K_H\right]\frac{1}{h_3}\frac{\partial T_s}{\partial\xi_3}\Bigg\}.\end{aligned} \tag{13}$$

Note that in both Eqs. (11) and (13) above, the inclusion of the diffusivities inside the derivatives allows them to be made spatially variable, which may be desirable for either physical or numerical reasons.

(*c*) *Eddy-induced transport.* Gent and McWilliams [19] and Gent *et al.* [20] have parameterised the unresolved tracer transports due to the nonlinear effects of subgrid scale eddies as an advection of tracer by an eddy-induced transport velocity $\mathbf{u}^*$. In the latter paper, this is taken to be proportional to the gradient of the logarithm of the thickness of

(locally referenced) potential density intervals, $\partial z/\partial p$, and hence to the vertical gradient of the isopycnal slope. The form proposed by Gent *et al.* [20] is

$$\mathbf{u}_{\mathrm{H}}^{*} = -\partial(A_E\mathbf{S})/\partial z, \qquad w^{*} = \boldsymbol{\nabla}_{\mathrm{H}} \cdot (A_E\mathbf{S}), \tag{14}$$

the two expressions being related by continuity. A_E may be interpreted as a 'thickness diffusivity' and has been absorbed into the derivative to ensure nondivergence of the depth-integrated horizontal transport. Eddy-induced velocities normal to ocean boundaries are made zero by setting $A_E\mathbf{S} = 0$ at the boundaries.

Griffies [24] has pointed out that the eddy-induced advective term may be rewritten as a diffusive term, which can be obtained by the easily verified manipulation

$$\begin{aligned} -\boldsymbol{\nabla} \cdot (\mathbf{u}^{*}T_s) &= -\boldsymbol{\nabla}_{\mathrm{H}} \cdot \left(-\frac{\partial A_E\mathbf{S}}{\partial z}T_s\right) - \frac{\partial}{\partial z}(\boldsymbol{\nabla}_{\mathrm{H}} \cdot (A_E\mathbf{S})T_s) \\ &= \boldsymbol{\nabla}_{\mathrm{H}} \cdot \left(-A_E\mathbf{S}\frac{\partial T_s}{\partial z}\right) + \frac{\partial}{\partial z}(A_E\mathbf{S} \cdot \boldsymbol{\nabla}_{\mathrm{H}}T_s). \end{aligned}$$

The terms imply the addition of an antisymmetric or skew diffusivity tensor to the symmetrical isopycnal diffusivity tensor ($\mathsf{K}_{\mathrm{isop}}$) given in Eq. (12), viz.,

$$\begin{aligned} &\begin{bmatrix} 0 & 0 & -A_E S_x \\ 0 & 0 & -A_E S_y \\ A_E S_x & A_E S_y & 0 \end{bmatrix} + \mathsf{K}_{\mathrm{isop}} \\ &\quad = \begin{bmatrix} A_I + A_H & 0 & (A_I - A_E)S_x \\ 0 & A_I + A_H & (A_I - A_E)S_y \\ (A_I - A_E)S_x & (A_I + A_E)S_y & A_I\left(S_x^2 + S_y^2\right) + K_H \end{bmatrix}. \end{aligned} \tag{15}$$

In addition to simplifying the calculation, especially in the case where $A_E = A_I$, when $K_{13} = K_{23} = 0$, this formulation has some numerical advantages, which are discussed in Appendix E.

2.6. *Hydrostatic Pressure Gradient Term*

The hydrostatic pressure is obtained by integration of the *in situ* density, calculated from the equation of state, viz.,

$$\tilde{p} = -\int_0^z \rho g \, dz' = -\int_0^{\xi_3} \rho g h_3 \, d\xi_3'. \tag{16}$$

Horizontal gradients are calculated from

$$-\frac{1}{\rho}\boldsymbol{\nabla}_{\mathrm{H}}\tilde{p} = -\frac{1}{\rho_0}\sum_{m=1}^{2}\frac{1}{h_m}\frac{\partial \tilde{p}}{\partial \xi_m}\hat{\mathbf{e}}_m, \tag{17}$$

where a constant density, ρ_0, is used in the Boussinesq approximation.

2.7. *Advective Term for Momentum*

Using the identity $\boldsymbol{\nabla}\cdot(\mathbf{uu}) \equiv (\mathbf{u}\cdot\boldsymbol{\nabla}\mathbf{u}) + \mathbf{u}\boldsymbol{\nabla}\cdot\mathbf{u}$, and the fact that an incompressible ocean is nondivergent, the momentum advection term can be written in flux form and evaluated using the formula for the divergence of a tensor (Eq. A6), which in this case is the open product, **uu**, viz.,

$$
\begin{aligned}
-\mathbf{u}\cdot\boldsymbol{\nabla}\mathbf{u} &= -\boldsymbol{\nabla}\cdot(\mathbf{uu}) \\
&= -\left\{\frac{1}{h_1h_2}\left[\frac{\partial}{\partial\xi_1}(h_2u_1u_1) + \frac{\partial}{\partial\xi_2}(h_1u_2u_1) + u_2u_1\frac{\partial h_1}{\partial\xi_2} - u_2u_2\frac{\partial h_2}{\partial\xi_1}\right] + \frac{1}{h_3}\frac{\partial}{\partial\xi_3}(u_3u_1)\right\}\hat{\mathbf{e}}_1 \\
&\quad -\left\{\frac{1}{h_1h_2}\left[\frac{\partial}{\partial\xi_1}(h_2u_1u_2) + \frac{\partial}{\partial\xi_2}(h_1u_2u_2) + u_1u_2\frac{\partial h_2}{\partial\xi_1} - u_1u_1\frac{\partial h_1}{\partial\xi_2}\right] + \frac{1}{h_3}\frac{\partial}{\partial\xi_3}(u_3u_2)\right\}\hat{\mathbf{e}}_2 \\
&\quad -\left\{\frac{1}{h_1h_2}\left[\frac{\partial}{\partial\xi_1}(h_2u_1u_3) + \frac{\partial}{\partial\xi_2}(h_1u_2u_3)\right] + \frac{1}{h_3}\frac{\partial}{\partial\xi_3}(u_3u_3)\right\}\hat{\mathbf{e}}_3. \qquad (18)
\end{aligned}
$$

Vertical velocity is calculated diagnostically and its advection (the $\hat{\mathbf{e}}_3$ component) is not considered. The $\hat{\mathbf{e}}_1$ and $\hat{\mathbf{e}}_2$ components of the momentum advection are each composed of the following parts: the first two terms are the *scalar-calculated* horizontal advective terms, i.e., calculated without reference to the rotation of the base vectors; the second two are the horizontal advective metric terms; and the last is the vertical advection of horizontal momentum. The metric terms take rotation into account by means of two grid-dependent coefficients, $L_1 = 1/(h_1h_2)\,\partial h_1/\partial\xi_2$ and $L_2 = 1/(h_1h_2)\,\partial h_2/\partial\xi_1$, which are proportional to the divergence of grid lines in the meridional and zonal directions, respectively. In spherical coordinates, $L_1 = -\tan\phi/(a\delta\lambda)$, but $L_2 = 0$, since the parallels do not converge.

2.8. *Friction Term*

Williams [67], Wajsowicz [62], and Smagorinsky [55] have derived the form of the friction term in spherical polar coordinates by applying Phillips' [47] approximation of a shallow atmosphere (in which the Earth's radius is represented by a constant, a, in the formulae for the metric coefficients) to the tensor forms of the transverse isotropic stress–strain rate relationships. However, the full expansion of the friction term in orthogonal curvilinear coordinates was not given by these authors and is accordingly derived here. The term is first derived in terms of strain rates; this has also recently been done in a somewhat different fashion by Griffies and Hallberg [26]. It is further shown how the friction term can be usefully rewritten in a 'momentum diffusion' form analogous to that used in spherical coordinates by Bryan [6].

(*a*) *Strain rate components in curvilinear coordinates.* The expressions for strain rate in orthogonal curvilinear coordinates are of the form (*vide* [4], Appendix 2)

$$
\begin{aligned}
e_{11} &= \frac{1}{h_1}\frac{\partial u_1}{\partial\xi_1} + \frac{u_2}{h_1h_2}\frac{\partial h_1}{\partial\xi_2} + \frac{u_3}{h_1h_3}\frac{\partial h_1}{\partial\xi_3}, \\
e_{12} &= \frac{h_2}{2h_1}\frac{\partial}{\partial\xi_1}\left(\frac{u_2}{h_2}\right) + \frac{h_1}{2h_2}\frac{\partial}{\partial\xi_2}\left(\frac{u_1}{h_1}\right).
\end{aligned}
$$

Because in transverse curvilinear coordinates some of the metric derivatives are zero (Eq. A3), the components of the strain rate tensor simplify to

$$e_{11} = \frac{1}{h_1}\frac{\partial u_1}{\partial \xi_1} + \frac{u_2}{h_1 h_2}\frac{\partial h_1}{\partial \xi_2}, \qquad e_{12} = \frac{h_2}{2h_1}\frac{\partial}{\partial \xi_1}\left(\frac{u_2}{h_2}\right) + \frac{h_1}{2h_2}\frac{\partial}{\partial \xi_2}\left(\frac{u_1}{h_1}\right),$$
$$e_{22} = \frac{1}{h_2}\frac{\partial u_2}{\partial \xi_2} + \frac{u_1}{h_1 h_2}\frac{\partial h_2}{\partial \xi_1}, \qquad e_{13} = \frac{1}{2h_3}\frac{\partial u_1}{\partial \xi_3}\left[+\frac{1}{2h_1}\frac{\partial u_3}{\partial \xi_1}\right],$$
$$e_{33} = \frac{1}{h_3}\frac{\partial u_3}{\partial \xi_3}, \qquad e_{23} = \frac{1}{2h_3}\frac{\partial u_2}{\partial \xi_3}\left[+\frac{1}{2h_2}\frac{\partial u_3}{\partial \xi_2}\right].$$

Since the horizontal gradients of vertical velocity are very small in large-scale ocean applications, the bracketed terms in the expressions for e_{13} and e_{23} will be neglected from this point on. It is convenient to express the horizontal strain rate components in terms of the tension and shearing rates of deformation or strain,

$$\begin{aligned} D_T = e_{11} - e_{22} &= \frac{1}{h_1}\frac{\partial u_1}{\partial \xi_1} + \frac{u_2}{h_1 h_2}\frac{\partial h_1}{\partial \xi_2} - \frac{1}{h_2}\frac{\partial u_2}{\partial \xi_2} - \frac{u_1}{h_1 h_2}\frac{\partial h_2}{\partial \xi_1} \\ &= \frac{h_2}{h_1}\frac{\partial}{\partial \xi_1}\left(\frac{u_1}{h_2}\right) - \frac{h_1}{h_2}\frac{\partial}{\partial \xi_2}\left(\frac{u_2}{h_1}\right), \\ D_s = 2e_{12} &= \frac{h_2}{h_1}\frac{\partial}{\partial \xi_1}\left(\frac{u_2}{h_2}\right) + \frac{h_1}{h_2}\frac{\partial}{\partial \xi_2}\left(\frac{u_1}{h_1}\right). \end{aligned}$$

(*b*) *Form of the stress–strain rate relation.* The stress–strain rate relation for a fluid transversely isotropic with respect to the vertical coordinate, ξ_3, is of the following form, given by Williams [67], following Green and Zerna [23]:

$$\begin{bmatrix} \tau_{11} \\ \tau_{22} \\ \tau_{33} \\ \tau_{23} \\ \tau_{13} \\ \tau_{12} \end{bmatrix} = \begin{bmatrix} C_1 & C_2 & C_3 & 0 & 0 & 0 \\ C_2 & C_1 & C_3 & 0 & 0 & 0 \\ C_3 & C_3 & C_4 & 0 & 0 & 0 \\ 0 & 0 & 0 & C_5 & 0 & 0 \\ 0 & 0 & 0 & 0 & C_5 & 0 \\ 0 & 0 & 0 & 0 & 0 & (C_1 - C_2)/2 \end{bmatrix} \begin{bmatrix} e_{11} \\ e_{22} \\ e_{33} \\ 2e_{23} \\ 2e_{13} \\ 2e_{12} \end{bmatrix}.$$

(Note that the stresses here are in 'kinematic units,' i.e., the physical stresses divided by ρ.) Kirwan [31], Williams [67], and Wajsowicz [62] have shown that, in an incompressible fluid, constraints on the normal strain rates and deviatoric stresses,

$$e_{11} + e_{22} + e_{33} = \boldsymbol{\nabla} \cdot \mathbf{u} = 0,$$
$$\tau_{11} + \tau_{22} + \tau_{33} = 0,$$

reduce the number of independent eddy viscosities from 5 to 3: the familiar horizontal and vertical eddy viscosities,

$$A_M = (C_1 - C_2)/2, \qquad K_M = C_5,$$

and a third viscosity, variously defined as

$$\epsilon = K_2 = C_3 - C_2 \qquad [31, 67] \quad \text{and} \quad \nu = (C_1 + C_2)/2 - C_3 = A_M - \epsilon \qquad [62].$$

In fact, the normal stress equation alone effects this reduction, since the equation

$$\tau_{11} + \tau_{22} + \tau_{33} = (C_1 + C_2 + C_3)\boldsymbol{\nabla} \cdot \mathbf{u} + (C_3 + C_4 - C_1 - C_2)e_{33} = 0$$

imposes two constraints on the coefficients (viz., $C_1 + C_2 + C_3 = 0$ and $C_3 + C_4 - C_1 - C_2 = 0$), as recognised by Smagorinsky [55], making $\nu = 3/2\,(C_1 + C_2)$. His normal stress–strain relations can be rendered using A_M, K_M, and ν $(= 3 \times \text{his}\,\alpha)$ as

$$\begin{aligned}
\tau_{11} &= A_M(e_{11} - e_{22}) + \nu\left(\frac{1}{3}\boldsymbol{\nabla} \cdot \mathbf{u} - e_{33}\right), \\
\tau_{22} &= -A_M(e_{11} - e_{22}) + \nu\left(\frac{1}{3}\boldsymbol{\nabla} \cdot \mathbf{u} - e_{33}\right), \\
\tau_{33} &= -2\nu\left(\frac{1}{3}\boldsymbol{\nabla} \cdot \mathbf{u} - e_{33}\right).
\end{aligned} \tag{19}$$

The stress–strain rate relationships required in the friction term, after applying the incompressibility condition to and rearranging the first two equations above, may be written

$$\begin{aligned}
(\tau_{11} + \tau_{22})/2 &= -\nu e_{33}, \\
(\tau_{11} - \tau_{22})/2 &= A_M(e_{11} - e_{22}) = A_M D_T, \\
\tau_{12} &= A_M \cdot 2e_{12} = A_M D_S, \\
\tau_{13} &= K_M \cdot 2e_{13}, \\
\tau_{23} &= K_M \cdot 2e_{23}.
\end{aligned} \tag{20}$$

(*c*) *Curvilinear form of the friction term.* The frictional force is computed from the divergence of the eddy viscosity stress tensor, $\mathsf{T} = [\tau_{mn}]$, i.e.,

$$\rho\mathbf{F} = \boldsymbol{\nabla} \cdot (\rho\mathsf{T}).$$

It is appropriate to apply the Boussinesq approximation at this point, allowing ρ to be eliminated from both sides of the equation. Only the horizontal components, F_1 and F_2, figure in the equations of motion, and are given (from Eq. A6) by

$$\begin{aligned}
F_1 &= \frac{1}{h_1 h_2}\left[\frac{\partial}{\partial\xi_1}(h_2\tau_{11}) + \frac{\partial}{\partial\xi_2}(h_1\tau_{21}) + \tau_{21}\frac{\partial h_1}{\partial\xi_2} - \tau_{22}\frac{\partial h_2}{\partial\xi_1}\right] + \frac{1}{h_3}\frac{\partial\tau_{31}}{\partial\xi_3}, \\
F_2 &= \underbrace{\frac{1}{h_1 h_2}\left[\frac{\partial}{\partial\xi_1}(h_2\tau_{12}) + \frac{\partial}{\partial\xi_2}(h_1\tau_{22}) + \tau_{12}\frac{\partial h_2}{\partial\xi_1} - \tau_{11}\frac{\partial h_1}{\partial\xi_2}\right]}_{\mathbf{F}_\mathrm{H}} + \underbrace{\frac{1}{h_3}\frac{\partial\tau_{32}}{\partial\xi_3}}_{\mathbf{F}_\mathrm{V}}.
\end{aligned} \tag{21}$$

Since T is symmetric, only the τ_{12}, τ_{13}, and τ_{23} off-diagonal elements will hence be referred to. It is convenient to reexpress the normal stresses in $\mathbf{F}_\mathrm{H}$ in terms of their sum and difference.

For the ξ_1 component,

$$
\begin{aligned}
(F_{\mathrm{H}})_1 &= \frac{1}{h_1 h_2}\left\{\frac{\partial}{\partial \xi_1}\left[h_2\left(\frac{\tau_{11}-\tau_{22}}{2}+\frac{\tau_{11}+\tau_{22}}{2}\right)\right]\right. \\
&\quad \left. + \frac{1}{h_1}\,\frac{\partial}{\partial \xi_2}\left(h_1^2\tau_{12}\right) + \frac{\partial h_2}{\partial \xi_1}\left(\frac{\tau_{11}-\tau_{22}}{2}-\frac{\tau_{11}+\tau_{22}}{2}\right)\right\} \\
&= \frac{1}{h_1 h_2}\left\{\frac{1}{h_2}\frac{\partial}{\partial \xi_1}h_2^2\left(\frac{\tau_{11}-\tau_{22}}{2}\right) + \frac{1}{h_1}\frac{\partial}{\partial \xi_2}\left(h_1^2\tau_{12}\right) + h_2\frac{\partial}{\partial \xi_1}\left(\frac{\tau_{11}+\tau_{22}}{2}\right)\right\}.
\end{aligned}
$$

Adding in the F_{v} term from Eq. (21) and substituting the stress–strain rate expressions from Eq. (20), the friction terms become

$$
\begin{aligned}
F_1 &= \frac{1}{h_1 h_2}\left\{\frac{1}{h_2}\frac{\partial}{\partial \xi_1}\left(h_2^2 A_M D_T\right) + \frac{1}{h_1}\frac{\partial}{\partial \xi_2}\left(h_1^2 A_M D_S\right)\right\} \\
&\quad - \frac{1}{h_1}\frac{\partial}{\partial \xi_1}(\nu e_{33}) + \frac{1}{h_3}\frac{\partial}{\partial \xi_3}(K_M \cdot 2e_{13}), \\
F_2 &= \frac{1}{h_1 h_2}\left\{\frac{1}{h_2}\frac{\partial}{\partial \xi_1}\left(h_2^2 A_M D_S\right) - \frac{1}{h_1}\frac{\partial}{\partial \xi_2}\left(h_1^2 A_M D_T\right)\right\} \\
&\quad - \frac{1}{h_2}\frac{\partial}{\partial \xi_2}(\nu e_{33}) + \frac{1}{h_3}\frac{\partial}{\partial \xi_3}(K_M \cdot 2e_{23}).
\end{aligned}
\tag{22}
$$

The second term in each expression is proportional to the gradient of $\tau_{11}+\tau_{22}$ and hence τ_{33}. Williams [67] has argued that since τ_{33} should be proportional to $\overline{w'w'}$ the associated eddy viscosity should be of the order of A_M in a highly convective regime but negligible in a stably stratified atmosphere or ocean. (Williams made this comment in relation to ϵ, but clearly this should be understood to be $\nu = (A_M - \epsilon)$, as it has been by Wajsowicz, who has supported her argument with a scale analysis.) Accordingly, it has been the practice in hydrostatic models to ignore this term, as is done here. With this modification, the horizontal parts of Eq. (22) are equivalent to Eqs. (A3) and (A4) of Griffies and Hallberg [26], but with the density dependence suppressed.

Substituting the expressions for the strain rate in Eq. (22) with the ν terms removed,

$$
\begin{aligned}
F_1 &= \frac{1}{h_1 h_2}\left\{\frac{1}{h_2}\frac{\partial}{\partial \xi_1}\left\{h_2^2 A_M\left[\frac{h_2}{h_1}\frac{\partial}{\partial \xi_1}\left(\frac{u_1}{h_2}\right) - \frac{h_1}{h_2}\frac{\partial}{\partial \xi_2}\left(\frac{u_2}{h_1}\right)\right]\right\}\right. \\
&\quad \left. + \frac{1}{h_1}\frac{\partial}{\partial \xi_2}\left\{h_1^2 A_M\left[\frac{h_2}{h_1}\frac{\partial}{\partial \xi_1}\left(\frac{u_2}{h_2}\right) + \frac{h_1}{h_2}\frac{\partial}{\partial \xi_2}\left(\frac{u_1}{h_1}\right)\right]\right\}\right\} + \frac{1}{h_3}\frac{\partial}{\partial \xi_3}\left(\frac{K_M}{h_3}\frac{\partial u_1}{\partial \xi_3}\right), \\
F_2 &= \frac{1}{h_1 h_2}\left\{\frac{1}{h_2}\frac{\partial}{\partial \xi_1}\left\{h_2^2 A_M\left[\frac{h_2}{h_1}\frac{\partial}{\partial \xi_1}\left(\frac{u_2}{h_2}\right) + \frac{h_1}{h_2}\frac{\partial}{\partial \xi_2}\left(\frac{u_1}{h_1}\right)\right]\right\}\right. \\
&\quad \left. - \frac{1}{h_1}\frac{\partial}{\partial \xi_2}\left\{h_1^2 A_M\left[\frac{h_2}{h_1}\frac{\partial}{\partial \xi_1}\left(\frac{u_1}{h_2}\right) - \frac{h_1}{h_2}\frac{\partial}{\partial \xi_2}\left(\frac{u_2}{h_1}\right)\right]\right\}\right\} + \frac{1}{h_3}\frac{\partial}{\partial \xi_3}\left(\frac{K_M}{h_3}\frac{\partial u_2}{\partial \xi_3}\right).
\end{aligned}
\tag{23}
$$

The friction term may be used either as given above or in the reorganised form given in (e) below. In either case, the viscosities, being within the derivatives, may be made variable.

(*d*) *Nonlinear mixing.* Horizontal eddy viscosities in ocean models normally have to be made rather unphysically large in order to satisfy overall stability criteria; however, they may be reduced in most places if the local velocity field be taken into account. Smagorinsky [54] scaled the viscosity to the horizontal deformation; his Eq. 4.2.2 corresponds to Eq. (22) above but specialised to the case of a conformal (Mercator) grid (his $m = 1/h_1 = 1/h_2$) and a viscosity parameterised as

$$A_M = (k_H \Delta)^2 D_P,$$

where k_H is a nondimensional number (0.28 in his model), Δ is a mixing length, and

$$D_P = \sqrt{D_T^2 + D_S^2}$$

is a grid-invariant quantity known as the 'pure' or 'total' deformation rate. In his scheme, the tracer diffusivity, A_H, was parameterised with the same dependence. In a later paper [55], he provided the physical basis of the parameterisation and a tabulation of the many different values corresponding to k_H that have been used by other modellers.

For numerical reasons, Δ is usually related to the grid scale, e.g., $\Delta = \sqrt{h_1 h_2}$ or $\Delta = \max(h_1, h_2)$. Because the grid size normally differs in the two coordinate directions, Rosati and Miyakoda [51] and others have scaled the viscosities in the x and y directions anisotropically, viz.,

$$\tau_{11} = (A_M)_x D_T \qquad \tau_{12} = (A_M)_y D_S,$$
$$\tau_{21} = (A_M)_x D_S \qquad \tau_{22} = -(A_M)_y D_T,$$

where $(A_M)_x = (k_H h_1)^2 D_P$ and $(A_M)_y = (k_H h_2)^2 D_P$; however, it should be noted that this prescription violates the requirement that $\tau_{21} = \tau_{12}$ (i.e., that the stress tensor be symmetric, and hence irrotational) and the nonconvective assumption that $\tau_{33} = 0$, since

$$\tau_{11} + \tau_{22} = -\tau_{33} = [(A_M)_x - (A_M)_y] D_T.$$

(*e*) *Momentum diffusion form of the friction term.* An alternative form of the friction term may be obtained from a manipulation of the horizontal parts of Eq. (23) (see Appendix B); this may be written

$$(F_{\mathrm{H}})_1 = \boldsymbol{\nabla} \cdot (A_M \boldsymbol{\nabla} u_1) + \left(M_1 \frac{\partial u_2}{\partial \xi_1} - M_2 \frac{\partial u_2}{\partial \xi_2} \right) + (N_1 u_1 + N_2 u_2),$$
$$(F_{\mathrm{H}})_2 = \boldsymbol{\nabla} \cdot (A_M \boldsymbol{\nabla} u_2) - \underbrace{\left(M_1 \frac{\partial u_1}{\partial \xi_1} - M_2 \frac{\partial u_1}{\partial \xi_2} \right)}_{\text{1st metric term}} + \underbrace{(N_1 u_2 - N_2 u_1)}_{\text{2nd metric term}}, \tag{24}$$

where

$$M_1 = \frac{1}{h_1 h_2} \left(\frac{2A_M}{h_1} \frac{\partial h_1}{\partial \xi_2} + \frac{\partial A_M}{\partial \xi_2} \right),$$
$$M_2 = \frac{1}{h_1 h_2} \left(\frac{2A_M}{h_2} \frac{\partial h_2}{\partial \xi_1} + \frac{\partial A_M}{\partial \xi_1} \right),$$

$$N_1 = \frac{1}{h_1 h_2}\left[-\frac{1}{h_2}\frac{\partial}{\partial \xi_1}\left(A_M \frac{h_2}{h_1}\frac{\partial h_2}{\partial \xi_1}\right) - \frac{1}{h_1}\frac{\partial}{\partial \xi_2}\left(A_M \frac{h_1}{h_2}\frac{\partial h_1}{\partial \xi_2}\right)\right],$$

$$N_2 = \frac{1}{h_1 h_2}\left[+\frac{1}{h_2}\frac{\partial}{\partial \xi_1}\left(A_M \frac{h_2}{h_1}\frac{\partial h_1}{\partial \xi_2}\right) - \frac{1}{h_1}\frac{\partial}{\partial \xi_2}\left(A_M \frac{h_1}{h_2}\frac{\partial h_2}{\partial \xi_1}\right)\right].$$

In spherical coordinates, where all metric derivatives with respect to longitude are zero, the coefficients reduce to the forms derived by Murray and Reason [39] from the more general equations of Wajsowicz [62], and in the constant viscosity case, to the form incorporated in the model of Bryan [6]. In curvilinear coordinates with constant viscosity, the coefficients reduce to forms equivalent to the somewhat more complex expressions (when expanded) derived by Smith *et al.* [57].

The first term in each equation is the scalar-calculated Fickian diffusion of momentum; the bracketed expressions which follow are what we shall call the first and second order metric terms. An interpretation of the metric terms is possible in the constant viscosity case. The first order metric terms take account of the rotation of the base vectors between neighbouring points in the x and y directions respectively. In spherical coordinates this only occurs in the x direction. The second order metric terms are proportional to velocities that are of like and contrary name to the momentum component in which they are resolved. The like-named (N_1) components take account of the curving apart of the meridians and/or parallels, one or the other of which will always occur on a doubly curved surface. The contrary-named (N_2) components are present when cell aspect ratios have a two-dimensional dependence which cannot be removed by separate one-dimensional compressions; it may be shown that this property does not exist in conformal or stretched–conformal grids (such as the spherical grid, or the bipolar, confocal, or multipolar grids of Murray [38]) but may become appreciable where subgrids of different properties have been patched or graded together.

In the above manipulations, it was possible to remove the mixed derivatives, $\partial^2 u_1/\partial\xi_1\partial\xi_2$ and $\partial^2 u_2/\partial\xi_1\partial\xi_2$, which, in a finite difference calculation for a point (i, j), are the only ones requiring velocity values at the four corner points, $(i \pm 1, j \pm 1)$ of a nine-point template. With their removal, the friction term only requires a five-point Laplacian template but has complicated coefficients. When viscosities are constant in time, then so are the coefficients, and their complexity is of no moment, since they can be calculated once and for all at the beginning of the integration. But when viscosities are parameterised as in the Smagorinsky scheme, strain rates are needed for calculating them even if they are not used in the friction operator; moreover, the metric term coefficients, being functions of the viscosity gradients, must still be computed at each time step. There is thus nothing to be gained from the manipulation in terms of computational speed when this scheme is used; however, there is another consideration. As discussed by Smith *et al.* [57], the five-point operator has the advantage over the nine-point operator that it does not contain a checkerboard null-space and is thereby able to damp noise at the grid scale. However, two-grid intervals are eliminated in the manipulation only to the extent that they arise as an essential part of the strain-based numerics; they survive in the first metric terms when there is grid curvilinearity (which is present in both curvilinear and spherical coordinates) and/or viscosity variation. The relative sizes of the two sources of computational mode are probably proportional to the sizes of the main and first metric terms, and hence to the maximum wave numbers of, respectively, the velocity variation (the grid scale) on the one hand and the grid curvature or viscosity variation on the other. When the curvature is small (as it is usually designed to be on most curvilinear grids) and the viscosity variation, if allowed, is likewise small (as it is likely

to be when the viscosity is based on grid size), both having an inverse length scale of order $1/a$, the second source will also be small and probably easily stabilised by the horizontal viscosity of the main or 'Laplacian' term. When strain-dependent mixing is implemented, both sources will be on the scale of the velocity variation, so it is not certain how effective the stabilisation will be. This question probably warrants investigation. A formulation which obviates all sources of null mode has recently been proposed by Griffies and Hallberg [26] and embodies numerics similar to those implemented for isopycnal diffusion by Griffies *et al.* [25].

2.9. *Stream Function Tendency*

Taking the curl of the external mode equation (Eq. 7) to eliminate the pressure gradient term results in

$$\mathbf{k}\cdot\boldsymbol{\nabla}\times\left[\frac{\delta_{2t}\bar{\mathbf{u}}}{2\delta t_{\mathrm{uv}}}+\alpha f\mathbf{k}\times\delta_{2t}\bar{\mathbf{u}}\right]=\overline{G_z}, \tag{25}$$

where

$$\overline{G_z}=\mathbf{k}\cdot\boldsymbol{\nabla}\times\overline{\mathbf{G_u}}=\frac{1}{h_1h_2}\left[\frac{\partial}{\partial\xi_1}(h_2\overline{G_v})-\frac{\partial}{\partial\xi_2}(h_1\overline{G_u})\right] \tag{26}$$

is the vorticity forcing, written in curvilinear form with the aid of Eq. (A2). The fact that the depth-averaged flow is nondivergent allows the velocity to be represented as a stream function, ψ, viz.,

$$\bar{\mathbf{u}}=\frac{1}{H}\mathbf{k}\times\boldsymbol{\nabla}\psi=\frac{1}{H}\left(-\frac{1}{h_2}\frac{\partial\psi}{\partial\xi_2},\frac{1}{h_1}\frac{\partial\psi}{\partial\xi_1},0\right), \tag{27}$$

where H is the ocean depth. Substituting this in the first term on the LHS of Eq. (25) gives

$$\mathbf{k}\cdot\boldsymbol{\nabla}\times\frac{\delta_{2t}\bar{\mathbf{u}}}{2\delta t_{\mathrm{uv}}}=\frac{1}{h_1h_2}\left[\frac{\partial}{\partial\xi_1}\left(\frac{1}{H}\frac{h_2}{h_1}\frac{\partial\psi^t}{\partial\xi_1}\right)+\frac{\partial}{\partial\xi_2}\left(\frac{1}{H}\frac{h_1}{h_2}\frac{\partial\psi^t}{\partial\xi_2}\right)\right], \tag{28}$$

where $\psi^t=\delta_{2t}\psi/2\delta t_{\mathrm{uv}}$ is the time-discretised form of the stream function tendency. If the Coriolis term is treated semiimplicitly, the second term is also needed,

$$\begin{aligned}\mathbf{k}\cdot\boldsymbol{\nabla}\times(\alpha f\mathbf{k}\times\delta_{2t}\bar{\mathbf{u}})&=-\alpha(2\delta t_{\mathrm{uv}})\mathbf{k}\cdot\boldsymbol{\nabla}\times\left(\frac{f}{H}\boldsymbol{\nabla}\psi^t\right)\\&=-\frac{\alpha(2\delta t_{\mathrm{uv}})}{h_1h_2}\left[\frac{\partial}{\partial\xi_1}\left(h_2\frac{f}{H}\frac{1}{h_2}\frac{\partial}{\partial\xi_2}\psi^t\right)-\frac{\partial}{\partial\xi_2}\left(h_1\frac{f}{H}\frac{1}{h_1}\frac{\partial}{\partial\xi_1}\psi^t\right)\right]\\&=-\frac{\alpha(2\delta t_{\mathrm{uv}})}{h_1h_2}\left[\frac{\partial}{\partial\xi_1}\left(\frac{f}{H}\right)\cdot\frac{\partial\psi^t}{\partial\xi_2}-\frac{\partial}{\partial\xi_2}\left(\frac{f}{H}\right)\cdot\frac{\partial\psi^t}{\partial\xi_1}\right].\end{aligned} \tag{29}$$

Substituting Eqs. (26), (28), and (29) in (25) gives an elliptical equation in ψ^t, which may be solved using any one of a number of relaxation methods.

3. FINITE DIFFERENCE EQUATIONS

3.1. Grid Operations

On the Arakawa B grid, scalars lie at integral points in each horizontal direction, and the velocity components lie at half integral points, i.e., at the corners of each tracer cell. Because fractional subscripts cannot be used in programming, it has been the practice in the spherical model to distinguish integral and half-integral one-dimensional coordinate and metric arrays by the suffixes 't,' for tracer, and 'u' for velocity, respectively. In curvilinear models, positions and metric factors are functions of two indices, each of which may assume integral or half-integral values, and thus need to be defined on four subgrids, which, by way of respect to the convention outlined above, may be designated by the suffixes, 'tt,' 'ut,' 'tu,' or 'uu,' the first letter referring to the ξ direction and the second to the η direction; thus,

$$\lambda_{tt}(i, j) = \lambda_{ij}, \qquad \phi_{ut}(i, j) = \phi_{i+\frac{1}{2},j}.$$

In the spherical model, t-cell coordinates are commonly obtained as averages of adjacent u-cell coordinates. The concept of 't-centring' has little meaning in the case of curvilinear models, where grid orientation and spacing both vary in two dimensions; instead, the practice that we have adopted is to obtain the points of the four subgrids from a smooth double resolution grid created directly by the grid generation algorithm, as recommended by Marti *et al.* [36]. While geographical positions are only needed for determining metric and Coriolis factors at model initialisation, the double suffix notation is useful to indicate the centring of quantities which appear in the model equations, e.g., T_{tt}, u_{uu}, $(A_H)_{tu}$, etc. The horizontal grid conventions are illustrated in Fig. 1.

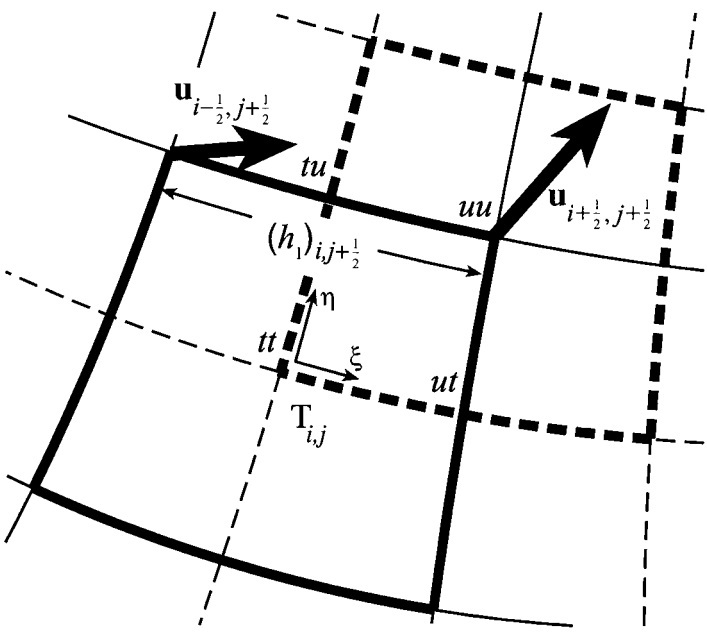

FIG. 1. Horizontal grid arrangement, showing coordinate axes at (i, j), locations of tt, ut, tu, and uu subgrids, t-cell (solid) and u-cell (dashed) boundaries, and sample variables.

In the discrete forms of the model equations, derivatives are calculated with the aid of centred differencing and averaging operators, e.g.,

$$(\delta_\xi q)_t(i, j) = (\delta_\xi q)_{i,j} = q_{i+\frac{1}{2},j} - q_{i-\frac{1}{2},j} = q_u(i, j) - q_u(i-1, j),$$
$$(\overline{q}^{\xi})_u(i, j) = (\overline{q}^{\xi})_{i+\frac{1}{2},j} = \frac{1}{2}(q_{i+1,j} + q_{i,j}) = \frac{1}{2}[q_t(i+1, j) + q_t(i, j)].$$

(To minimise multiple subscripting, the unsubscripted forms of grid variables and velocity components, ξ, η, ζ, u, v, and w, have been used in this section.) The above usages are readily extended to two dimensions. Because both averaging and differencing operations result in a quantity referenced to a grid position (in ξ or η) half an index unit from its progenitors, it is not always necessary to specify what value of i or j it refers to, but only to know upon which of the four subgrids it is located. The operators for a two-dimensional quantity behave as

$$\delta_\xi q_{tt} = (\delta_\xi q)_{ut}, \qquad \overline{q_{ut}}^{\eta} = (\overline{q}^{\eta})_{uu},$$

and they may be applied consecutively, viz.,

$$\delta_\xi \delta_\eta q_{tt} = \delta_\eta \delta_\xi q_{tt} = (\delta_\xi \delta_\eta q)_{uu},$$
$$\overline{\delta_\eta q_{tt}}^{\xi} = \delta_\eta \overline{q_{tt}}^{\xi} = (\delta_\eta \overline{q}^{\xi})_{uu},$$
$$\delta_\xi \delta_\xi q_{tt} = (\delta_\xi \delta_\xi q)_{tt}.$$

A consecutive averaging and differencing in the same direction results in a difference over a double interval,

$$\overline{\delta_\xi q_{tt}}^{\xi} = \delta_\xi \overline{q_{tt}}^{\xi} = \frac{1}{2}(q_{i+1,j} - q_{i,j} + q_{i,j} - q_{i-1,j}) = \frac{1}{2}\delta_{2\xi} q_{tt} = \frac{1}{2}(\delta_{2\xi} q)_{tt},$$

where $(\delta_{2\alpha} x)_i = \alpha_{i+1} - \alpha_{i-1}$.

The vertical discretisation is the same as for the spherical model, with prognostic quantities being computed at integral or t levels (cell centres) and vertical velocities and fluxes at half-integral or w levels (cell interfaces). Vertical coordinates are referenced to 't' and 'w' grids using a single suffix, e.g.,

$$z_t(k) = z_k, \qquad z_w(k) = z_{k+\frac{1}{2}} \quad (z_w(0) = z_{\frac{1}{2}} = 0),$$

and model quantities using three suffixes, where necessary, e.g., T_{ttt} ($\equiv T_{tt}$), u_{uut} ($\equiv u_{uu}$), w_{ttw}, w_{uuw}, $(K_M)_{uuw}$, etc. Note that, while k increases downward, differences are taken in the upward direction; thus,

$$(\delta_\zeta q)_{k+\frac{1}{2}} = q_k - q_{k+1}.$$

Some ancillary issues related to grid operations are discussed in the appendices. Methods of supplying grid information to the model and of interpolating data on input and output are given in Appendix C, and conditions for continuity at various types of reentrant array boundary are given in Appendix D.

3.2. Velocity and the Continuity Equation

The horizontal velocity is reconstituted from two parts: a barotropic part, calculated from the stream function, and a baroclinic part, $\mathbf{u}'$, viz.,

$$u_{uu} = \frac{-1}{(h_2 H)_{uu}} \delta_\eta \overline{\psi_{tt}}^{\xi} + u'_{uu}, \qquad v_{uu} = \frac{1}{(h_1 H)_{uu}} \delta_\xi \overline{\psi_{tt}}^{\eta} + v'_{uu}.$$

The depth at 'u' points (H_{uu}) is taken as that of the shallowest of the four 't' points surrounding it. These velocities are averaged to cell faces in the continuity and advection equations; however, at velocity cell faces, the *advecting* (but not *advected*) velocity can be calculated without averaging of the barotropic part using

$$u_{tu}^{\text{adv}} = \frac{-1}{(h_2 H)_{tu}} \delta_\eta \psi_{tt}, + \overline{u'_{uu}}^{\xi}, \qquad v_{ut}^{\text{adv}} = \frac{1}{(h_1 H)_{ut}} \delta_\xi \psi_{tt}, + \overline{v'_{uu}}^{\eta},$$

where $H_{i,j+\frac{1}{2}} = \max(H_{i+\frac{1}{2},j+\frac{1}{2}}, H_{i-\frac{1}{2},j+\frac{1}{2}})$, etc.

Vertical velocity is calculated from the continuity equation (Eq. 9). This is required for both tracers and vectors, and must be computed at 'ttw' and 'uuw' points. The material fluxes, $\mathcal{F}_u = h_2 u$ and $\mathcal{F}_v = h_1 v$, are intermediate quantities used in the continuity and advection calculations.

For tracers:

$$\boldsymbol{\nabla} \cdot \mathbf{u} = \frac{1}{(h_1 h_2)_{tt}} \{\delta_\xi (\mathcal{F}_u)_{ut} + \delta_\eta (\mathcal{F}_v)_{tu}\} + \frac{1}{(h_3)_t} \delta_\zeta w_{ttw} = 0,$$

where $(\mathcal{F}_u)_{ut} = \overline{(h_2)_{uu} u_{uu}}^{\eta}$, $(\mathcal{F}_v)_{tu} = \overline{(h_1)_{uu} v_{uu}}^{\xi}$. The inclusion of the scale factors inside the averages (rather than as $(h_2)_{ut}$ and $(h_1)_{tu}$ outside the averages) makes the advecting velocity a weighted average; this needs to be done in order to ensure conservation of mechanical energy when work is done by pressure gradient forces, as shown for spherical coordinates by Pacanowski ([43], Sections 8.5 and 9.3) and for curvilinear coordinates in Appendix E. The vertical velocity is given by

$$\begin{aligned} w_{i,j,k+\frac{1}{2}} &= w_{i,j,k-\frac{1}{2}} + (h_3)_k (\boldsymbol{\nabla}_{\mathrm{H}} \cdot \mathbf{u})_{i,j,k}, \\ w_{i,j,\frac{1}{2}} &= w_{i,j,k_{\text{bot}}+\frac{1}{2}} = 0. \end{aligned}$$

For velocities:

$$\boldsymbol{\nabla} \cdot \mathbf{u} = \frac{1}{(h_1 h_2)_{uu}} \{\delta_\xi (\mathcal{F}_u)_{tu} + \delta_\eta (\mathcal{F}_v)_{ut}\} + \frac{1}{(h_3)_t} \delta_\zeta w_{uuw} = 0.$$

where $(\mathcal{F}_u)_{tu} = (h_2)_{tu} u_{tu}^{\text{adv}}$, $(\mathcal{F}_v)_{ut} = (h_1)_{ut} v_{ut}^{\text{adv}}$. The vertical velocity is given by

$$\begin{aligned} w_{i+\frac{1}{2},j+\frac{1}{2},k+\frac{1}{2}} &= w_{i+\frac{1}{2},j+\frac{1}{2},k-\frac{1}{2}} + (h_3)_k (\boldsymbol{\nabla}_{\mathrm{H}} \cdot \mathbf{u})_{i+\frac{1}{2},j+\frac{1}{2},k}, \\ w_{i+\frac{1}{2},j+\frac{1}{2},\frac{1}{2}} &= w_{i+\frac{1}{2},j+\frac{1}{2},k_{\text{bot}}+\frac{1}{2}} = 0. \end{aligned}$$

3.3. Tendency Terms

(*a*) *Advective Term for Tracers*

$$-\mathbf{u} \cdot \boldsymbol{\nabla} T = -\frac{1}{(h_1 h_2)_{tt}} \left\{ \delta_\xi \left[(\mathcal{F}_u)_{ut} \overline{T_{tt}}^{\xi} \right] + \delta_\eta \left[(\mathcal{F}_v)_{tu} \overline{T_{tt}}^{\eta} \right] \right\} - \frac{1}{(h_3)_t} \delta_\zeta \left(w_{ttw} \overline{T_{ttt}}^{\zeta} \right).$$

(*b*) *Diffusive Term for Tracers*

Horizontal mixing

$$\boldsymbol{\nabla}\cdot(\mathsf{K}\boldsymbol{\nabla}T) = \frac{1}{(h_1h_2)_{tt}}\left\{\delta_\xi\left[\left(A_H\frac{h_2}{h_1}\right)_{ut}\delta_\xi T_{tt}\right] + \delta_\eta\left[\left(A_H\frac{h_1}{h_2}\right)_{tu}\delta_\eta T_{tt}\right]\right\} + \frac{1}{(h_3)_t}\delta_\zeta\left[\frac{(K_H)_{ttw}}{(h_3)_w}\delta_\zeta T_{ttt}\right].$$

Isopycnal mixing. The Cox [13] discretisation of the diffusion term with isopycnal mixing is

$$\begin{aligned}\boldsymbol{\nabla}\cdot(\mathsf{K}\boldsymbol{\nabla}T) = {}& \frac{1}{(h_1h_2)_{tt}}\left\{\delta_\xi\left[(h_2)_{ut}\left((A_I+A_H)_{utt}\frac{1}{(h_1)_{ut}}\delta_\xi T_{tt}+(A_IS_x)_{utt}\frac{1}{(h_3)_t}\delta_\zeta\overline{T_{ttt}}^{\xi\zeta}\right)\right]\right.\\ &\left.+\delta_\eta\left[(h_1)_{tu}\left((A_I+A_H)_{tut}\frac{1}{(h_2)_{tu}}\delta_\eta T_{tt}+(A_IS_y)_{tut}\frac{1}{(h_3)_t}\delta_\zeta\overline{T_{ttt}}^{\eta\zeta}\right)\right]\right\}\\ &+\frac{1}{(h_3)_t}\delta_\zeta\left\{(A_IS_x)_{ttw}\frac{1}{(h_1)_{tt}}\delta_\xi\overline{T_{ttt}}^{\xi\zeta}+(A_IS_y)_{ttw}\frac{1}{(h_2)_{tt}}\delta_\eta\overline{T_{ttt}}^{\eta\zeta}\right\}\\ &+\frac{1}{(h_3)_t}\delta_\zeta\left\{\left[A_I\left(S_x^2+S_y^2\right)+K_H\right]_{ttw}\frac{1}{(h_3)_w}\delta_\zeta T_{ttt}\right\}. \end{aligned} \tag{30}$$

The term on the last line is the K_{33} component, which may need to be calculated implicitly, for reasons given below.

Cox [13] has shown that the numerical stability requirement, $K_{mn} \le h_m h_n/4(\delta t_{\mathrm{ts}})_k$, places constraints on the maximum permissible isopycnal slope,

$$S \le \sqrt{\frac{K_{33}}{A_I}} = \frac{(h_3)_k}{2\sqrt{A_I(\delta t_{\mathrm{ts}})_k}},$$
$$S \le \frac{K_{13}}{A_I} \sim \frac{K_{23}}{A_I} \sim \frac{K_{31}}{A_I} \sim \frac{K_{32}}{A_I} \sim \frac{h_{\mathrm{H}}(h_3)_k}{4A_I(\delta t_{\mathrm{ts}})_k},$$

where h_{H} is a characteristic horizontal grid length, $(h_3)_k$ is the thickness of the level k where the slope is calculated, and $(\delta t_{\mathrm{ts}})_k$ is the (accelerated) tracer time step for level k. The first constraint is the more severe but may be avoided by treating the whole of the K_{33} term implicitly. When constant isopycnal diffusivity is used, the second constraint normally limits the slopes used in the off-diagonal terms to about $1/200$ near the surface and $1/20$ in the deep ocean. The slopes $(\rho_x/\hat{\rho}_z)$ and $(\rho_y/\hat{\rho}_z)$ are effectively limited by a minimum condition placed on the magnitude of a modified vertical density gradient,

$$-\hat{\rho}_z = \min[-\rho_z, \sqrt{\rho_x^2+\rho_y^2}/(\text{max. slope})],$$

and are calculated as

$$(S_x) = -\rho_x\hat{\rho}_z/\left(\hat{\rho}_z^2+\epsilon\right), \qquad (S_y) = -\rho_y\hat{\rho}_z/\left(\hat{\rho}_z^2+\epsilon\right), \tag{31}$$

where ϵ is a small number to prevent overflows. As slopes are required at 'utt,' 'tut,' and 'ttw' points, and all three density gradients are required for each slope calculation, nine

gradients are required; these are computed in a manner analogous to that used in the GFDL model, as follows:

$$(\rho_x)_{utt} = \frac{1}{(h_1)_{ut}}\delta_\xi \rho_{ttt}, \quad (\rho_y)_{utt} = \frac{1}{(h_2)_{ut}}\delta_\eta \overline{\rho_{ttt}}^{\xi\eta}, \quad (\rho_z)_{utt} = \frac{1}{(h_3)_t}\delta_\zeta \overline{\rho_{ttt}}^{\xi\zeta},$$
$$(\rho_x)_{tut} = \frac{1}{(h_1)_{tu}}\delta_\xi \overline{\rho_{ttt}}^{\eta\xi}, \quad (\rho_y)_{tut} = \frac{1}{(h_2)_{tu}}\delta_\eta \rho_{ttt}, \quad (\rho_z)_{tut} = \frac{1}{(h_3)_t}\delta_\zeta \overline{\rho_{ttt}}^{\eta\zeta},$$
$$(\rho_x)_{ttw} = \frac{1}{(h_1)_{tt}}\delta_\xi \overline{\rho_{ttt}}^{\zeta\xi}, \quad (\rho_y)_{ttw} = \frac{1}{(h_2)_{tt}}\delta_\eta \overline{\rho_{ttt}}^{\zeta\eta}, \quad (\rho_z)_{ttw} = \frac{1}{(h_3)_w}\delta_\zeta \rho_{ttt}.$$

As slope limiting has the effect of creating spurious horizontal (and hence diapycnal) diffusion, an alternative way of applying the constraint is to limit A_I where slopes are steep, as has been done by Gerdes *et al.* [22] and Danabasoglu and McWilliams [14].

The Cox scheme is normally stabilised with a background component of horizontally oriented diffusion. The 'background' diffusivity is commonly set to a value of about half that of the isopycnal diffusivity, which greatly detracts from its modelling advantages. Griffies *et al.* [25] have shown that the Cox scheme is inherently unstable because it does not prevent upgradient diffusive fluxes along isopycnals and because fluxes of the active tracers are not balanced so as to ensure zero fluxes of potential density. They have proposed an alternative numerical formulation which overcomes these problems and have implemented it in Version 3 of the modular ocean model. Because of the complexity of the coding, the present authors have not adapted the Griffies *et al.* formulation to curvilinear coordinates at this stage.

Eddy-induced transport. When eddy-induced transport is parameterised by the Gent–McWilliams scheme, the effective 'material' fluxes used for calculating continuity and advection of tracers are determined from the total transport velocity, which is the sum of the large scale velocity, **u**, and the eddy-induced transport velocity, $\mathbf{u}^*$, i.e.,

$$\begin{aligned}(\mathcal{F}_u)_{ut} &= \overline{(h_2)_{uu}u_{uu}}^{\eta} + (h_2)_{ut}u^*_{ut},\\ (\mathcal{F}_v)_{tu} &= \overline{(h_1)_{uu}v_{uu}}^{\xi} + (h_1)_{tu}v^*_{tu}.\end{aligned} \tag{32}$$

The eddy-induced velocities are calculated from

$$u^*_{ut} = -\delta_\zeta (A_E S_x)_{utw}/(h_3)_t,$$
$$v^*_{tu} = -\delta_\zeta (A_E S_y)_{tuw}/(h_3)_t.$$

The slopes are computed from appropriately centred density gradients using Eq. (31), but they are not necessarily limited in the same way as in the isopycnal mixing term. The x- and y-directed density gradients are averaged from those used in the isopycnal mixing calculation,

$$(\rho_x)_{utw} = \overline{(\rho_x)_{utt}}^{\zeta}, \quad (\rho_y)_{utw} = \overline{(\rho_y)_{utt}}^{\zeta}, \quad (\rho_z)_{utw} = \overline{(\rho_z)_{ttw}}^{\xi},$$
$$(\rho_x)_{tuw} = \overline{(\rho_x)_{tut}}^{\zeta}, \quad (\rho_y)_{tuw} = \overline{(\rho_y)_{tut}}^{\zeta}, \quad (\rho_z)_{tuw} = \overline{(\rho_z)_{ttw}}^{\eta}.$$

Boundary conditions are satisfied by setting $(A_E S_x)_{utw}$ and $(A_E S_y)_{tuw}$ to zero at surface and land boundaries of 't' grid cells.

Eddy-induced transport can also be parameterised as a skew diffusive flux, as proposed by Griffies [24]. While recommending its implementation in conjunction with the Griffies *et al.* [25] isopycnal diffusion scheme, he also noted that it could profitably be used with Cox's [13] numerics. Following Eq. (15), this can easily be done by substituting $(A_I - A_E)$ for A_I in the K_{13} and K_{23} diffusivity tensor components and $(A_I + A_E)$ for A_I in the K_{31} and K_{32} components in Eq. (30).

(*c*) *Hydrostatic Pressure Gradient Term*

$$-\frac{1}{\rho}\nabla_{\mathrm{H}}\tilde{p} = -\frac{1}{\rho_0}\left[\frac{1}{(h_1)_{uu}}\delta_\xi\,\overline{\tilde{p}_{ttt}}^{\eta},\ \frac{1}{(h_2)_{uu}}\delta_\eta\,\overline{\tilde{p}_{ttt}}^{\xi},\ 0\right]$$

Here, $\tilde{p}_{ttt} = \tilde{p}_{i,j,k}$ is the hydrostatic pressure, calculated from

$$\begin{aligned}\tilde{p}_{i,j,1} &= g[\rho_{i,j,1}(h_3)_1]/2,\\ \tilde{p}_{i,j,k} &= g[\rho_{i,j,k-1}(h_3)_{k-1} + \rho_{i,j,k}(h_3)_k]/2 + \tilde{p}_{i,j,k-1},\end{aligned}$$

where ρ is the *in situ* density (for accuracy, referenced in practice to an arbitrary level-dependent value, which has no effect on the horizontal gradients).

(*d*) *Advective Term for Momentum*

$$\begin{aligned}-(\mathbf{u}\cdot\nabla\mathbf{u})_1 = &-\frac{1}{(h_1h_2)_{uu}}\left\{\delta_\xi\left[(\mathcal{F}_u)_{tu}\,\overline{u_{uu}}^{\xi}\right] + \delta_\eta\left[(\mathcal{F}_v)_{ut}\,\overline{u_{uu}}^{\eta}\right]\right\}\\ &-(L_1u_{uu} - L_2v_{uu})v_{uu} - \frac{1}{(h_3)_t}\delta_\zeta\left[w_{uuw}\overline{u_{uu}}^{\zeta}\right], \qquad (33)\\ -(\mathbf{u}\cdot\nabla\mathbf{u})_2 = &-\frac{1}{(h_1h_2)_{uu}}\left\{\delta_\xi\left[(\mathcal{F}_u)_{tu}\overline{v_{uu}}^{\xi}\right] + \delta_\eta\left[(\mathcal{F}_v)_{ut}\overline{v_{uu}}^{\eta}\right]\right\}\\ &+(L_1u_{uu} - L_2v_{uu})u_{uu} - \frac{1}{(h_3)t}\delta_\zeta\left[w_{uuw}\overline{v_{uu}}^{\zeta}\right]. \qquad (34)\end{aligned}$$

$\mathcal{F}_u$ and $\mathcal{F}_v$ are as given in Section 3.2, and the multipliers in the metric terms are

$$L_1 = \frac{1}{(h_1h_2)_{uu}}\delta_\eta(h_1)_{ut}, \qquad L_2 = \frac{1}{(h_1h_2)_{uu}}\delta_\xi(h_2)_{tu}.$$

(*e*) *Friction Term*

$$F_m = (F_{\mathrm{H}})_m + \frac{1}{(h_3)_t}\delta_\zeta\left[\frac{(K_M)_{uuw}}{(h_3)_w}\delta_\zeta(u_m)_{uut}\right], \qquad m = 1, 2.$$

The horizontal part may be represented in terms of strain rates,

$$\begin{aligned}(F_{\mathrm{H}})_1 &= \frac{1}{\left(h_1h_2^2\right)_{uu}}\delta_\xi\left(h_2^2A_MD_T\right)_{tu} + \frac{1}{\left(h_1^2h_2\right)_{uu}}\delta_\eta\left(h_1^2A_MD_S\right)_{ut},\\ (F_{\mathrm{H}})_2 &= \frac{1}{\left(h_1h_2^2\right)_{uu}}\delta_\xi\left(h_2^2A_MD_S\right)_{tu} - \frac{1}{\left(h_1^2h_2\right)_{uu}}\delta_\eta\left(h_1^2A_MD_T\right)_{ut},\end{aligned}$$

where

$$(D_T)_{tu} = \left(\frac{h_2}{h_1}\right)_{tu} \delta_\xi\left(\frac{u}{h_2}\right)_{uu} - \left(\frac{h_1}{h_2}\right)_{tu} \delta_\eta\left[\frac{\overline{v_{uu}}^{\xi\eta}}{(h_1)_{tt}}\right],$$

$$(D_S)_{tu} = \left(\frac{h_2}{h_1}\right)_{tu} \delta_\xi\left(\frac{v}{h_2}\right)_{uu} + \left(\frac{h_1}{h_2}\right)_{tu} \delta_\eta\left[\frac{\overline{u_{uu}}^{\xi\eta}}{(h_1)_{tt}}\right],$$

$$(D_T)_{ut} = \left(\frac{h_2}{h_1}\right)_{ut} \delta_\xi\left[\frac{\overline{u_{uu}}^{\xi\eta}}{(h_2)_{tt}}\right] - \left(\frac{h_1}{h_2}\right)_{ut} \delta_\eta\left(\frac{v}{h_1}\right)_{uu},$$

$$(D_S)_{ut} = \left(\frac{h_2}{h_1}\right)_{ut} \delta_\xi\left[\frac{\overline{v_{uu}}^{\xi\eta}}{(h_2)_{tt}}\right] + \left(\frac{h_1}{h_2}\right)_{ut} \delta_\eta\left(\frac{u}{h_1}\right)_{uu}.$$

In the Smagorinsky scheme, the total deformation rates, and hence the viscosities, are also evaluated at 'ut' and 'tu' points, using the equations given in Section 2.8(d). Tracer diffusivities may be calculated in a similar fashion, except that the order in which the subscripts 'ut' and 'tu' appear in the equations will be reversed.

Alternatively, the momentum diffusion form may be used,

$$\begin{aligned}(F_{\mathrm{H}})_1 = {} & \frac{1}{(h_1h_2)_{uu}}\left\{\delta_\xi\left[\left(A_M\frac{h_2}{h_1}\right)_{tu}\delta_\xi(u_{uu})\right] + \delta_\eta\left[\left(A_M\frac{h_1}{h_2}\right)_{ut}\delta_\eta(u_{uu})\right]\right\} \\ & +(M_1/2)\,\delta_{2\xi}v_{uu} - (M_2/2)\,\delta_{2\eta}v_{uu} + N_1u_{uu} + N_2v_{uu}, \\ (F_{\mathrm{H}})_2 = {} & \frac{1}{(h_1h_2)_{uu}}\left\{\delta_\xi\left[\left(A_M\frac{h_2}{h_1}\right)_{tu}\delta_\xi(v_{uu})\right] + \delta_\eta\left[\left(A_M\frac{h_1}{h_2}\right)_{ut}\delta_\eta(v_{uu})\right]\right\} \\ & -(M_1/2)\,\delta_{2\xi}u_{uu} + (M_2/2)\,\delta_{2\eta}u_{uu} + N_1v_{uu} - N_2u_{uu},\end{aligned} \tag{35}$$

where

$$M_1 = \frac{1}{(h_1h_2)_{uu}}\left[\left(\frac{2A_M}{h_1}\right)_{uu}\delta_\eta(h_1)_{ut} + \delta_\eta(A_M)_{ut}\right],$$

$$M_2 = \frac{1}{(h_1h_2)_{uu}}\left[\left(\frac{2A_M}{h_2}\right)_{uu}\delta_\xi(h_2)_{tu} + \delta_\xi(A_M)_{tu}\right],$$

$$N_1 = \frac{1}{(h_1h_2)_{uu}}\left\{-\frac{1}{(h_2)_{uu}}\delta_\xi\left[\left(A_M\frac{h_2}{h_1}\right)_{tu}\delta_\xi(h_2)_{uu}\right] - \frac{1}{(h_1)_{uu}}\delta_\eta\left[\left(A_M\frac{h_1}{h_2}\right)_{ut}\delta_\eta(h_1)_{uu}\right]\right\},$$

$$N_2 = \frac{1}{(h_1h_2)_{uu}}\left\{+\frac{1}{(h_2)_{uu}}\delta_\xi\left[\left(A_M\frac{h_2}{h_1}\right)_{tu}\delta_\eta(h_1)_{tt}\right] - \frac{1}{(h_1)_{uu}}\delta_\eta\left[\left(A_M\frac{h_1}{h_2}\right)_{ut}\delta_\xi(h_2)_{tt}\right]\right\}.$$

These coefficients correspond to the continuous forms given in Section 2.8(e); however, M_1 and M_2 are divided by 2 in Eq. (35) because the velocity differences are taken over a double interval. When variable viscosities are used with these equations, A_M must be evaluated at ut, tu, and uu points and, if specified as a field at say uu points, it will need to be appropriately averaged, e.g., $(A_M)_{ut} = \overline{(A_M)_{uu}}^{\eta}$ and $\delta_\eta(A_M)_{ut} = \frac{1}{2}\delta_{2\eta}(A_M)_{uu}$.

3.4. Stream Function Calculation

The depth averaged vorticity forcing is calculated at tt points using Eq. (26),

$$(\overline{G_z})_{tt} = \frac{1}{(h_1h_2)_{tt}}\left\{\delta_\xi\left[\overline{(h_2)_{uu}(\overline{G_v})_{uu}}^{\eta}\right] - \delta_\eta\left[\overline{(h_1)_{uu}(\overline{G_u})_{uu}}^{\xi}\right]\right\}.$$

This is to be equated with an elliptical expression of the stream function tendency, ψ^t. Following the method used in the GFDL model, this function is computed from the stream function tendencies of a five-point Laplacian star, using a matrix of coefficients, C_E, C_W, C_N, C_S, and C_C, referring to the points 'east,' 'west,' 'north,' and 'south' of, and 'centred upon' the point at which the differential expression is to be evaluated. The elliptical expression given in Eq. (28) may be written

$$\begin{aligned}
\mathbf{k}\cdot\boldsymbol{\nabla}\times\frac{\delta_{2t}\bar{\mathbf{u}}}{2\delta t_{\mathrm{uv}}} &= \frac{1}{(h_1h_2)_{tt}}\left\{\delta_\xi\left[\left(\frac{1}{H}\frac{h_2}{h_1}\right)_{ut}\delta_\xi\psi^t_{tt}\right]+\delta_\eta\left[\left(\frac{1}{H}\frac{h_1}{h_2}\right)_{tu}\delta_\eta\psi^t_{tt}\right]\right\}\\
&= \frac{1}{(h_1h_2)_{i,j}}\left[\left(\frac{1}{H}\frac{h_2}{h_1}\right)_{i+\frac12,j}\left(\psi^t_{i+1,j}-\psi^t_{i,j}\right)-\left(\frac{1}{H}\frac{h_2}{h_1}\right)_{i-\frac12,j}\left(\psi^t_{i,j}-\psi^t_{i-1,j}\right)\right.\\
&\quad\left.+\left(\frac{1}{H}\frac{h_1}{h_2}\right)_{i,j+\frac12}\left(\psi^t_{i,j+1}-\psi^t_{i,j}\right)-\left(\frac{1}{H}\frac{h_1}{h_2}\right)_{i,j-\frac12}\left(\psi^t_{i,j}-\psi^t_{i,j-1}\right)\right]\\
&= C_E\psi^t_{i+1,j}+C_W\psi^t_{i-1,j}+C_N\psi^t_{i,j+1}+C_S\psi^t_{i,j-1}+C_C\psi^t_{i,j},
\end{aligned}$$

where

$$\begin{aligned}
C_E &= \frac{1}{(h_1h_2)_{i,j}}\left(\frac{1}{H}\frac{h_2}{h_1}\right)_{i+\frac12,j}, \qquad C_W = \frac{1}{(h_1h_2)_{i,j}}\left(\frac{1}{H}\frac{h_2}{h_1}\right)_{i-\frac12,j},\\
C_N &= \frac{1}{(h_1h_2)_{i,j}}\left(\frac{1}{H}\frac{h_1}{h_2}\right)_{i,j+\frac12}, \qquad C_S = \frac{1}{(h_1h_2)_{i,j}}\left(\frac{1}{H}\frac{h_1}{h_2}\right)_{i,j-\frac12},\\
C_C &= -(C_E+C_W+C_N+C_S),
\end{aligned}$$

and $H_{i+1/2,j} = (H_{i+1/2,j+1/2}+H_{i+1/2,j-1/2})/2$, etc., as in the GFDL model. For evaluating residuals, the coefficients at the central points are equally weighted; this is done by multiplying each of the coefficients in the star by the factor $1/C_C$.

In the semiimplicit treatment of the Coriolis term, the above expression is combined with

$$\begin{aligned}
\mathbf{k}\cdot\boldsymbol{\nabla}\times(\alpha f\mathbf{k}\times\delta_{2t}\bar{\mathbf{u}}) &= -\frac{\alpha(2\delta t_{\mathrm{uv}})}{(h_1h_2)_{tt}}\left[\overline{\delta_\xi\left(\frac{f}{H}\right)_{uu}\cdot\delta_\eta\psi^t_{tt}}^{\,\eta}-\overline{\delta_\eta\left(\frac{f}{H}\right)_{uu}\cdot\delta_\xi\psi^t_{tt}}^{\,\xi}\right]\\
&= -\frac{\alpha(2\delta t_{\mathrm{uv}})}{2(h_1h_2)_{i,j}}\left\{\left[\left(\frac{f}{H}\right)_{i+\frac12,j+\frac12}-\left(\frac{f}{H}\right)_{i-\frac12,j+\frac12}\right]\cdot\left(\psi^t_{i,j+1}-\psi^t_{i,j}\right)\right.\\
&\quad+\left[\left(\frac{f}{H}\right)_{i+\frac12,j-\frac12}-\left(\frac{f}{H}\right)_{i-\frac12,j-\frac12}\right]\cdot\left(\psi^t_{i,j}-\psi^t_{i,j-1}\right)\\
&\quad-\left[\left(\frac{f}{H}\right)_{i+\frac12,j+\frac12}-\left(\frac{f}{H}\right)_{i+\frac12,j-\frac12}\right]\cdot\left(\psi^t_{i+1,j}-\psi^t_{i,j}\right)\\
&\quad\left.-\left[\left(\frac{f}{H}\right)_{i-\frac12,j+\frac12}-\left(\frac{f}{H}\right)_{i-\frac12,j-\frac12}\right]\cdot\left(\psi^t_{i,j}-\psi^t_{i-1,j}\right)\right\}\\
&= C'_N\psi^t_{i,j+1}+C'_S\psi^t_{i,j-1}+C'_E\psi^t_{i+1,j}+C'_W\psi^t_{i-1,j}
\end{aligned}$$

(from Eq. 29) by allowing the coefficients

$$C'_E = \frac{\alpha(2\delta t)_{\text{uv}}}{2(h_1h_2)_{i,j}}\left[\left(\frac{f}{H}\right)_{i+\frac{1}{2},j+\frac{1}{2}} - \left(\frac{f}{H}\right)_{i+\frac{1}{2},j-\frac{1}{2}}\right],$$

$$C'_W = -\frac{\alpha(2\delta t)_{\text{uv}}}{2(h_1h_2)_{i,j}}\left[\left(\frac{f}{H}\right)_{i-\frac{1}{2},j+\frac{1}{2}} - \left(\frac{f}{H}\right)_{i-\frac{1}{2},j-\frac{1}{2}}\right],$$

$$C'_N = -\frac{\alpha(2\delta t)_{\text{uv}}}{2(h_1h_2)_{i,j}}\left[\left(\frac{f}{H}\right)_{i+\frac{1}{2},j+\frac{1}{2}} - \left(\frac{f}{H}\right)_{i-\frac{1}{2},j+\frac{1}{2}}\right],$$

$$C'_S = \frac{\alpha(2\delta t)_{\text{uv}}}{2(h_1h_2)_{i,j}}\left[\left(\frac{f}{H}\right)_{i+\frac{1}{2},j-\frac{1}{2}} - \left(\frac{f}{H}\right)_{i-\frac{1}{2},j-\frac{1}{2}}\right]$$

to augment the corresponding unprimed coefficients derived earlier. Note that the central coefficient, $C'_C = -(C'_E + C'_W + C'_N + C'_S)$, is easily seen to be zero.

The stream function tendency is obtained by extrapolating its field from the previous two time steps as a first guess and solving the elliptic equation,

$$\mathcal{L}\left(\psi^t_{i,j}\right) - (\overline{G_z})_{i,j} = 0.$$

4. COMPARISON OF ARCTIC SIMULATIONS

4.1. *Models and Grids*

Several simulations of the North Atlantic and Arctic Oceans were performed to compare aspects of the solutions in the northern high latitude regions produced by spherical and curvilinear coordinate models using a number of different horizontal grids. The spherical model is, with some additions, the latitude–longitude MOM1 [45] and is essentially a special case of the more general curvilinear model described in the preceeding sections.

Three grids were used, a 2.5° latitude × 4.0° longitude *spherical* grid and two curvilinear grids generated by methods described by Murray [38]. All grids were constructed globally and would normally be used in integrations employing the full global domain. However, because the focus of interest in the experiments described here is the grid-related differences in the representation of the Arctic Ocean, each grid was truncated at a grid row near 12.5°S so as to limit the model domain to just the Arctic and North Atlantic Oceans. The experiments therefore specifically exclude any consideration of differences affecting the other ocean basins or the Bering Strait throughflow. The high latitude parts of the grids used are shown in Fig. 2. For the main experiments, spherical and curvilinear grids were used with the respective models; however, for comparing their computational performance, both models were run using the spherical grid and small time steps to avoid the need for filtering, which is not available in the curvilinear model.

There are essentially two curvilinear configurations which give useful grid alignments in the Arctic region without causing too much distortion (and cell size variation) over the rest of the globe. The first has the northern grid pole displaced from the Arctic Ocean into one of the subpolar continents. This type is represented by a *bipolar* grid constructed by reprojecting the 2.5° × 4.0° spherical mesh so as to place the northern pole over Canada at 90°W, 60°N and the southern pole at 90°E, 85°S (Fig. 2b). Some latitudinal compression was applied

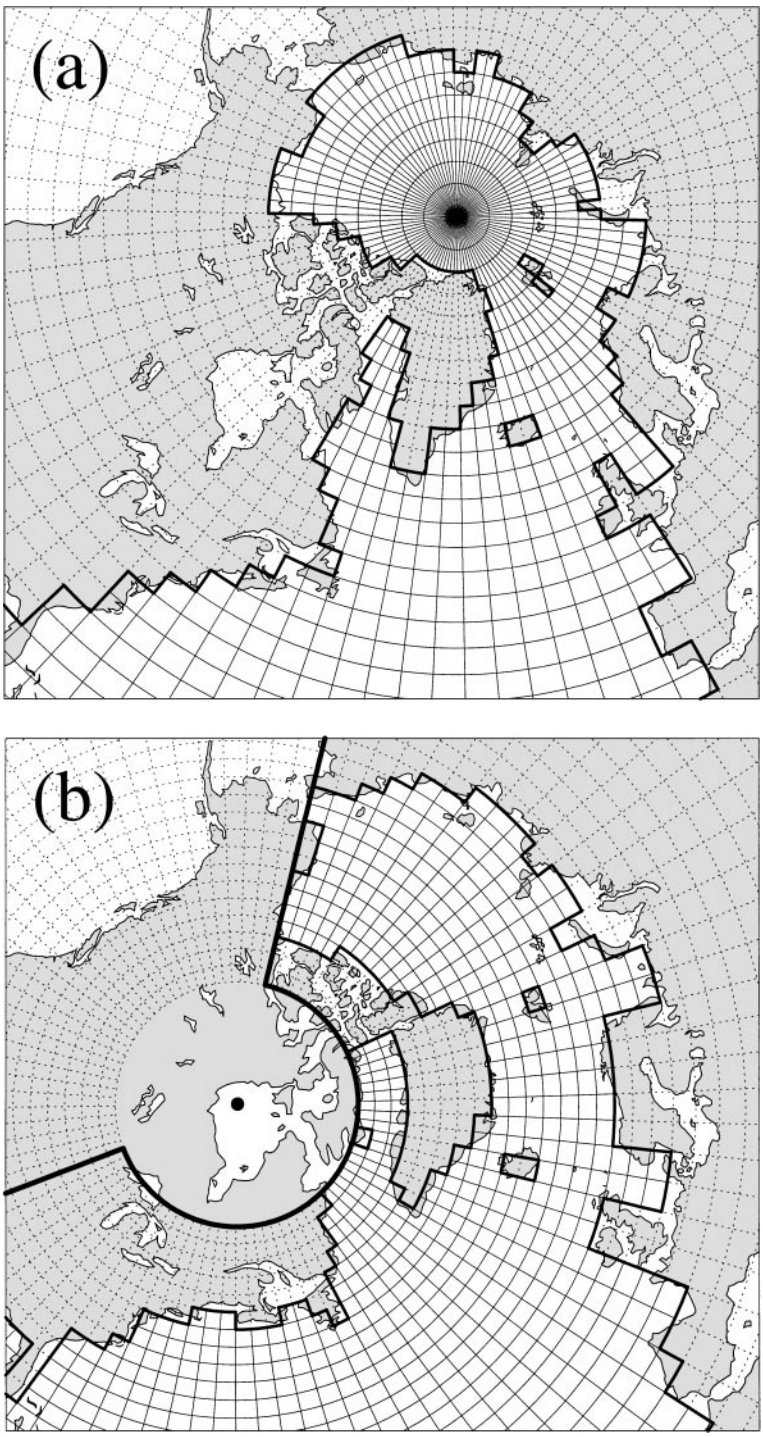

FIG. 2. Grids used for the North Atlantic simulations: (a) spherical grid (with North Pole a *t*-point), (b) bipolar grid, and (c) embedded grid. The cells of the full global grid array are shown in each case; however, only the truncated arrays were used in the integrations. In the curvilinear cases, (b) and (c), the limits of the truncated grids are indicated by heavy bold curves and the grid poles by black dots. Solid contours represent the boundaries of ocean *t* grid cells and dashed contours land cells. Note that the embedded grid is the same as the latitude–longitude grid south of 54°N.

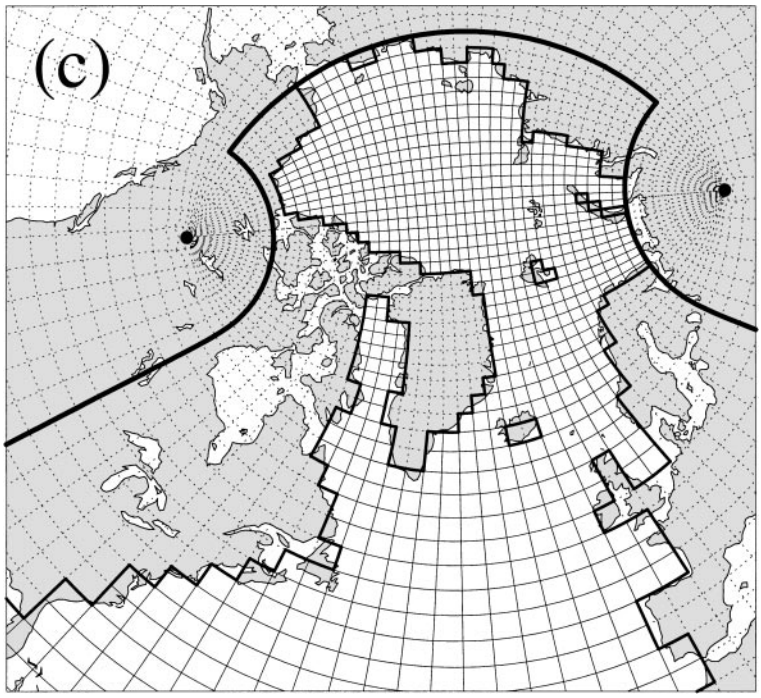

FIG. 2—*Continued*

near the northern pole in order to provide sufficient grid rows across the Greenland Sea. The grid was not designed to align contours with the equator, although this has been done, albeit with somewhat more distortion in the northern hemisphere, in the grids of Madec and Imbard [34] and Smith *et al.* [57].

In the second configuration, the single northern pole is replaced by two singularities symmetrically located over Canada and Siberia. The contours of such a grid can be constructed either from families of confocal conic sections on a north polar stereographic projection or by rotating and reprojecting one hemisphere of a spherical grid into the polar cap of a latitude–longitude grid. The latter method was used, giving an *embedded* grid in which the rotated hemisphere has poles at $-30^\circ \pm 90^\circ$E, 66°N and is joined smoothly over the latitude range 60°–70.8°N to a $2.5^\circ \times 4.0^\circ$ latitude–longitude grid covering the rest of the globe (Fig. 2c). This grid is essentially a transformation of the 'equatorial transform' grid of Eby and Holloway [17], but it has a smoothed transition at the join and the potential for a connection to the Pacific via the Bering Strait. Reprojection of the rotated hemisphere of the embedded grid into the region north of 66°N results in a natural decrease of grid meridional spacing toward the centre of the embedded region; this has the advantage of preventing large aspect ratios, which would have been produced had the meridional coordinate been rescaled to give a constant grid spacing along the rotated grid equator.

Other aspects of the two models were made as similar as possible for all horizontal grids. Twenty-one vertical levels were used, with thicknesses increasing from 25 to 450 m at depth. After interpolation, level masks were adjusted so that channels and ridges should be resolved in the same way on all grids. Denmark Strait, Faroe Bank Channel, and Fram Strait were made at least two tracer points wide at all levels above their sill depths (620, 800, and 2350 m), and the Lomonosov Ridge was given a depth of 1900 m. Each model

was forced with annual average Hellermann and Rosenstein [29] wind stresses, and tracers were restored using a 30-day time constant to 10 m Levitus [33] winter fields, enhanced in the Greenland and Labrador Seas to correct inadequacies in the data. A 50-day relaxation to climatology was applied at subsurface points along the southern boundary; however, this had little influence in the polar region. Horizontal and vertical viscosities were made constant at 3.5×10^9 and 20 $cm^2\ s^{-1}$, and horizontal friction was computed using the momentum diffusion discretisation (which, in spherical coordinates, is just the form normally used with constant viscosities in the GFDL model). Isopycnal diffusion and eddy-induced transport, implemented as a skew diffusion [24], were applied to tracers using Cox–Redi numerics, with isopycnal and thickness diffusivities $A_I = A_E = 1 \times 10^7\ cm^2\ s^{-1}$, and no background horizontal diffusivity was used. Vertical diffusivities were based on the profile of Kraus [32] and varied between $0.2\ cm^2\ s^{-1}$ near the surface and $1.4\ cm^2\ s^{-1}$ at 4150 m; the low surface values were considered appropriate in the Arctic Ocean, which is highly stratified in the upper layers.

Latitude–longitude integrations necessarily differ from curvilinear integrations in one important respect, the need for special modifications to overcome computational problems in the vicinity of the North Pole. This, of course, was one of the main motivations for implementing a curvilinear coordinate scheme. Nevertheless, to allow a fair comparison, we thought it important to choose a latitude–longitude formulation affected as little as possible by numerical artifacts. The problem of computing exchanges at the North Pole was solved by including a special prognostic calculation for a composite polar-tracer cell; this avoids the distortion caused by inserting an artificial island at the pole. The problem of small zonal grid spacing is normally solved by applying Fourier filtering. This circumvents the time step constraints, but the process of filtering does tend to degrade the solution somewhat. The best simulation, or at any rate the one most closely comparable to the curvilinear simulations, is achieved by running the model without filtering, but at the expense of an enormous increase in the number of iterations. For most studies, such an expense could not be contemplated; however, for the purposes of this demonstration, it would be possible to run an asynchronous 'equilibrium' integration without filtering. Because the time step implications are so great, we decided to run the latitude–longitude model both with and without filtering to help distinguish the effects of filtering from those of using different grids.

In the filtered experiment, Fourier filtering was applied north of a reference latitude of 80°N. The usual practice is to truncate Fourier components having a wavelength less than two grid intervals at the reference latitude; however, in this experiment, the truncation formula was modified so that the number of waves retained was given by

$$m \leq (n_i/\pi)\sin^{-1}(\cos\phi/\cos\phi_{\text{ref}}),$$

where n_i is the zonal periodicity and ϕ_{ref} is the filtering reference latitude. This has been recommended by Murray and Reason [40] on the grounds that it should maintain a constant time step limit for all rows in the filtering region, which is more efficient than using the standard truncation, which does not; it thereby obviates the need for tapering mixing coefficients downward near the pole, an expedient which introduces some artifacts of its own.

Each experiment was integrated for 80,000 days (220 years), with acceleration factors increasing this period by up to factors of eight at depth. In the curvilinear and filtered latitude–longitude integrations, both of which had an effective minimum grid length of a little less than 1°, the momentum time step was made 20 min and the tracer time step 2 days,

requiring 40,000 iterations. In the unfiltered latitude–longitude integration, the time steps had to be restricted to 1 min and 3 h, respectively, requiring 640,000 iterations.

4.2. *Results*

Figs. 3a–3c show the 139 m velocities for the spherical, bipolar, and embedded grid simulations. All plots show the same major currents, which in most cases correspond to those

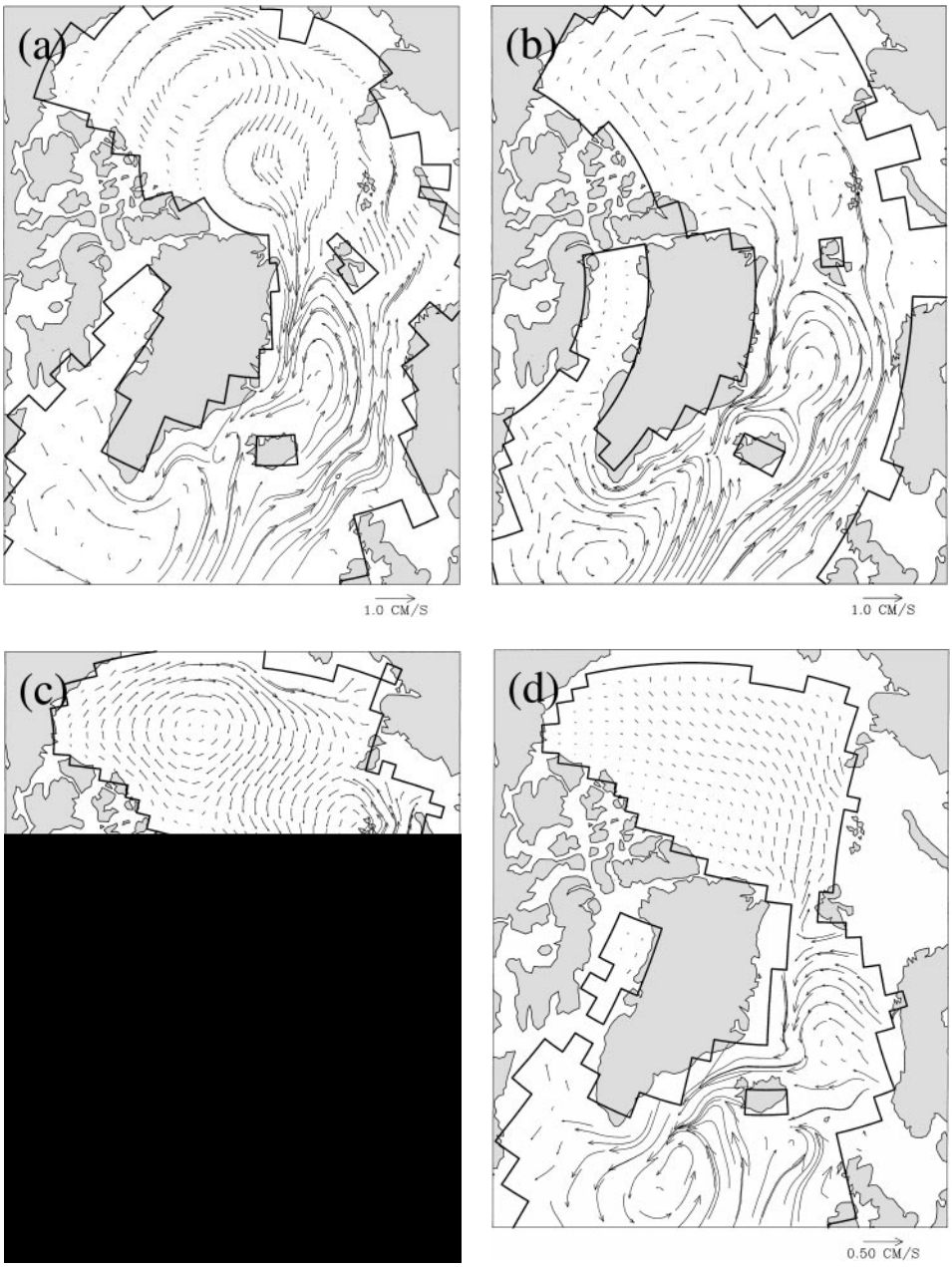

FIG. 3. Velocities at 139 m from simulations performed on the (a) spherical, (b) bipolar, and (c) embedded grids (450-day streamlines); also, (d) velocities at 545 m for the embedded grid simulation (900-day streamlines). The scale vectors are correct near the centre of the projection.

observed (see, e.g., [16, 46]). The main currents in the Arctic basin are the Beaufort Gyre and the Transpolar Drift Stream, which diverges from it and feeds into the East Greenland Current (EGC) and subsequently the Subpolar Gyre. The Beaufort Gyre occupies more of the Arctic than ice drift observations would suggest, and the Transpolar Drift Stream has been contorted into a double bend (cf., [10]). The North Atlantic Current enters the region from the south and branches into the Irminger Current, which merges with the Subpolar Gyre south of Iceland, and the Norwegian Current, which further divides, with a branch flowing east into the Barents Sea. The remainder of the Norwegian Current subsides and either merges with the EGC or undercuts it in the northward flowing West Spitsbergen Current (WSC). These subsurface currents are seen in the 545 m velocities, which are shown for just the embedded grid case in Fig. 3d; they are also present in the other simulations. The subducted Atlantic water is seen to spread out into the Arctic basin in a broad eastward-flowing counter-current. Evidence that this movement occurs in reality is provided by the presence of a warm tongue extending along the Siberian side of the ocean in the field of temperature at the depth of the temperature maximum [59]. The southward-flowing modelled current was intense in the Denmark Strait at the 545 m level, which is just above the sill, but diminished horizontally as the water overflowed into the depths of the Irminger Basin; the streamlines appear thus because they are integrated from the horizontal fields. At deeper levels (not shown); the flow in the Greenland and Norwegian Seas was predominantly southward toward and across the Faroe–Scotland Ridge.

The currents were rather weak in Fram Strait and relatively too strong in the Barents Sea. In these simulations, the EGC carried 1.4–1.6 Sv (1 Sv $\equiv 10^6$ m^3 s^{-1}) and the WSC 0.6–0.7 Sv, as compared to 3–5 Sv for each in the observations [59] and 4 Sv in horizontal mixing simulations, which we also performed. In the Barents Sea, the eastward transport of 0.8–1.0 Sv was of the right order, but the flow was too broad to correspond to the coast-following Murman Current and there was no feature corresponding to the west-flowing Percey Current on the Spitsbergen side. (By contrast, the horizontal mixing simulations did show a weak but cyclonic circulation.) The above defects are not wholly attributable to the use of eddy-induced transport. The currents flowing through Fram Strait are especially complex and are separated both vertically and horizontally, with currents at all levels flowing northward on the east side of the strait and southward on the west side [58]; this complexity is further compounded by the observation that the WSC divides into several branches, one of which recirculates into the EGC within the strait [48]. Because of the lateral viscosity and diffusivity necessary for computational stability, most numerical models cannot resolve currents which are closely separated in the horizontal, much less represent any recirculation within the strait; below about 500 m, Fram Strait is represented by only a single line of velocity points anyway. The consequences of this were that in the simulations (1) the WSC, which Aagaard *et al.* [2] found to contain two cores of $>3.5^\circ$C water between 50 and 200 m and within 200 km of Spitsbergen, was forced to flow wholly beneath the EGC and at depths exceeding 250 m, and (2) all southward transport was above this depth, thus precluding the saline outflow of deep Arctic Ocean water which Aagaard *et al.* [1] found over the Greenland continental slope and which they argued might be important for preconditioning convection in the Greenland Sea. Experiments with reduced lateral mixing coefficients ($A_M = 1.2 \times 10^9$ cm^2 s^{-1}, and $A_I = A_E = 0.5 \times 10^7$ cm^2 s^{-1} in the Arctic region) produced no change in this behaviour but did generate cyclonic gyres in the Siberian marginal seas and a closed cyclonic counter-gyre in the deeper levels of the Arctic Ocean.

Some vertical velocity fields are shown in Fig. 4. The important features implied by the horizontal velocity patterns are most clearly seen in those taken from the curvilinear

simulations. Fig. 4a is for the embedded grid experiment; the bipolar grid vertical velocities were similar. Downwelling was general in the Greenland Sea and affected both the East Greenland and Norwegian Currents. Subsidence also occurred where saline Atlantic water, cooled on passing through the Barents Sea, flowed off the Siberian Shelf. Throughout most of the Arctic there was weak upwelling, intensified somewhat around the boundaries. In the filtered latitude–longitude simulation, these features were almost completely disrupted by the noisy stellate pattern caused by Fourier filtering [40]. In the unfiltered simulation, this unwelcome behaviour was much reduced, but it is important to note that it persisted in the area between the pole and Fram Strait.

High densities in the Greenland Sea were encouraged by the cold saline surface restoration and hence positive surface density flux in that region (Fig. 5). In the Arctic the surface restoration was cold but fresh (reflecting the effect of the northern rivers and Bering throughflow) and, on balance, productive of low densities and stable stratification. The density patterns at 139 m differed little between grids and resembled one another better than the Levitus fields. Both model and Levitus fields show quantitatively similar patterns of high density in the centre of the Greenland Gyre and the Barents Sea, a density contrast in the southern Norwegian Sea, southward advection of lighter water in the EGC, and a pool of minimum densities in the Beaufort Sea. The isopycnals tended to follow the doubtful S-bend in the Transpolar Drift Stream in the model simulations, and densities were rather lower than observed in the eastern Arctic, probably as a result of the weak inflow of saline water through Fram Strait in the model. On the other hand, the rather suspicious radial structures about the pole in the Levitus data (somewhat smoothed out by interpolation to the curvilinear grid in Fig. 5c) appear to be the consequence of extrapolating from sparse data on a latitude–longitude grid in their analysis.

It may be that the velocity fields shown in Figs. 3a–3c look rather different from one another even though they show the same general features. If so, this has much to do with the different grid arrangements; the plots look much more similar when interpolated to the same grid. This certainly applies to the comparison of the embedded and spherical simulations. The differences between these are shown in Fig. 6a. Velocity differences were largest along the Greenland and Norwegian coasts and near the Siberian shelves; in these areas, they were mainly due to the local effects of topography on the interpolation or the somewhat more extended effects of differing channel geometry. Differences were very small in the central Arctic Ocean, where there is no shallow topography, and south of 60°, where the two grids become the same. The density differences at this level were greatest in the same areas as the velocity differences, and were mostly less than 0.2 sigma units. Considered beside this, the differences between the filtered and unfiltered simulations (Fig. 6b) were small and diminished quickly beyond the first few grid rows around the pole. Hence, the impact that filtering would have had on these *particular* spherical–curvilinear comparisons is fairly small; however, this would not necessarily apply in other types of model experiment.

The velocities in the bipolar simulation showed minor qualitative differences from those performed on the other two grids. The Subpolar Gyre was better defined and extended further into the Labrador Sea, as it does in reality. This was permitted by the greater north–south or grid zonal resolution of this grid near Canada. However, even with the mild compression applied at higher grid latitudes, the east–west resolution of this grid is correspondingly coarser, which resulted in poor resolution of currents in the Greenland Sea and required Fram Strait to be made very wide at depth in order to accommodate just a single row of velocity points. Because transports are mainly determined by other factors, the current

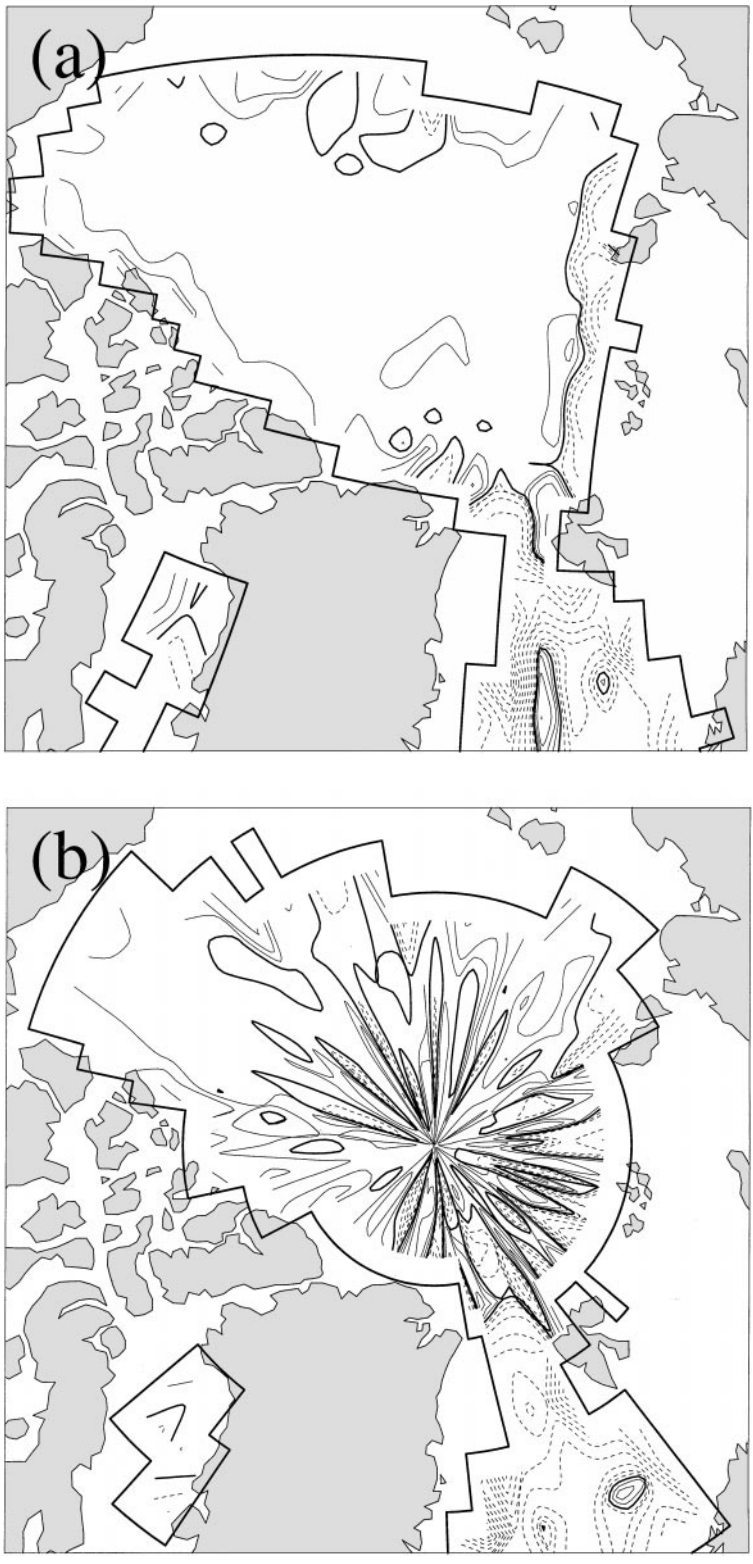

FIG. 4. Vertical velocities at 470 m for (a) embedded grid and (b) filtered and (c) unfiltered spherical grid models (contour interval 1×10^{-4} cm s^{-1}, with contours also at $\pm 0.25,\ 0.5 \times 10^{-4}$ cm s^{-1}).

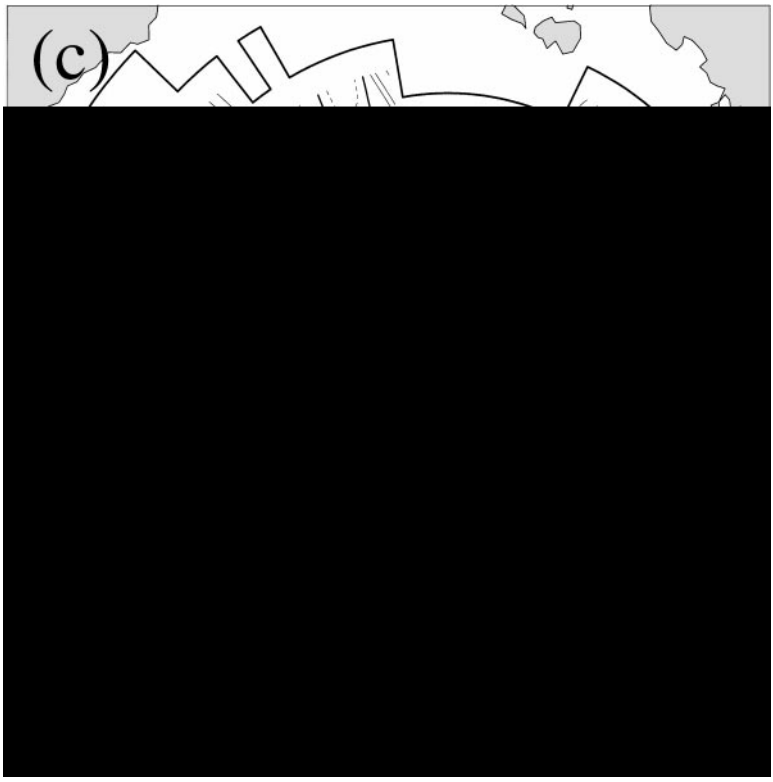

FIG. 4—*Continued*

velocities were lower than in the other simulations. Other current features which differed in this simulation were a considerable flow counterclockwise around the north of Iceland, which is not suggested by observations, and a slightly stronger flow through the Barents Sea.

The effects of the north–south exchanges can be seen in the potential temperature sections taken from the Norwegian Sea and across the pole in the Arctic along the meridian 2°E–178°W (Fig. 7). Both model and Levitus sections show a strong thermal stratification in the upper layers and an Atlantic layer temperature maximum at about 500 m in the Arctic (i.e., north of 80°). The maintenance of these features was aided by the actions of eddy-induced transport and low vertical diffusivities in the model; horizontal mixing simulations (not shown) represented them poorly. The local maximum indicated by the sloping closed contour near 78°N in some of the model sections is due to the westward movement of Atlantic water across them in the northern part of the Greenland Sea gyre and its subsidence in the WSC. This feature was not located so far north as in the observations, and this reflects the inadequate representation of the WSC. The form of the closed contour was best represented by the spherical model, possibly because of its greater zonal resolution, which allowed at least some slantwise separation of the north- and south-flowing current cores. Modelled temperatures in the Arctic Ocean proper were 0.6–0.8°C too high in both the Atlantic layer and at deeper levels. It is likely that the surface restoration was not providing a source of shelf water sufficiently cold and dense to penetrate the Atlantic layer and form Eurasian Basin bottom water in the manner hypothesized by Aagaard *et al.* [3]. The absence of such a water mass with the right properties would account for the absence of a modelled southward bottom current corresponding to the deep outflows through Fram Strait inferred by Smethie *et al.* [56] and Aagaard *et al.* [3].

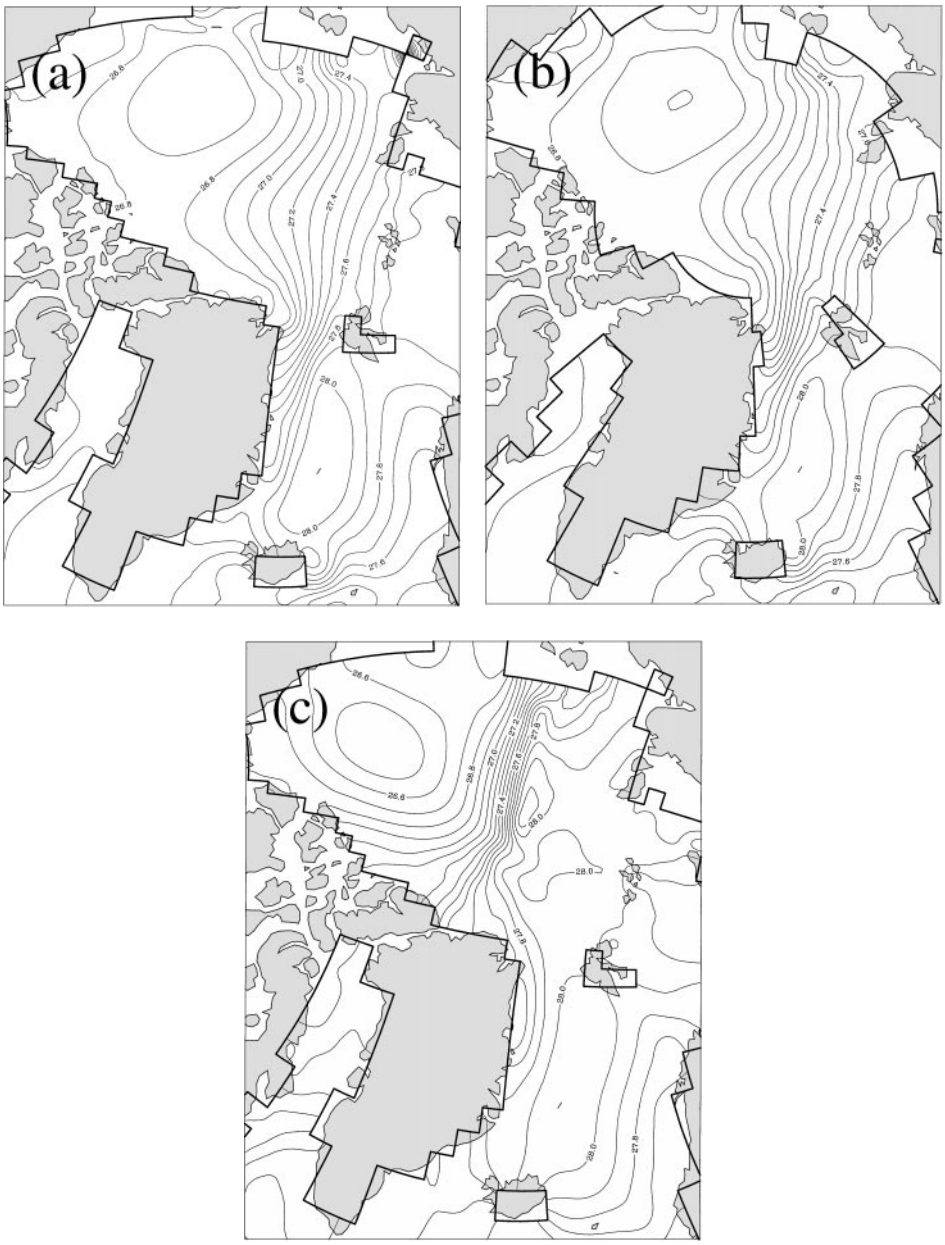

FIG. 5. Potential densities at 139 m from (a) the embedded grid model, (b) the unfiltered spherical grid model, and (c) the Levitus data (contour interval 0.1 sigma units).

5. CONCLUSION

In Sections 2 and 3, the spherical Bryan–Cox–Semtner model was generalised to accommodate orthogonal curvilinear coordinates. We emphasize the term 'generalised.' No changes were made to the dynamics, time stepping, or spatial finite differencing methods. The spherical model can thus be considered a special application of the curvilinear model. In practical terms, however, certain simplifications and differences in the centring of metric coefficients which are possible in the spherical model result in slight differences

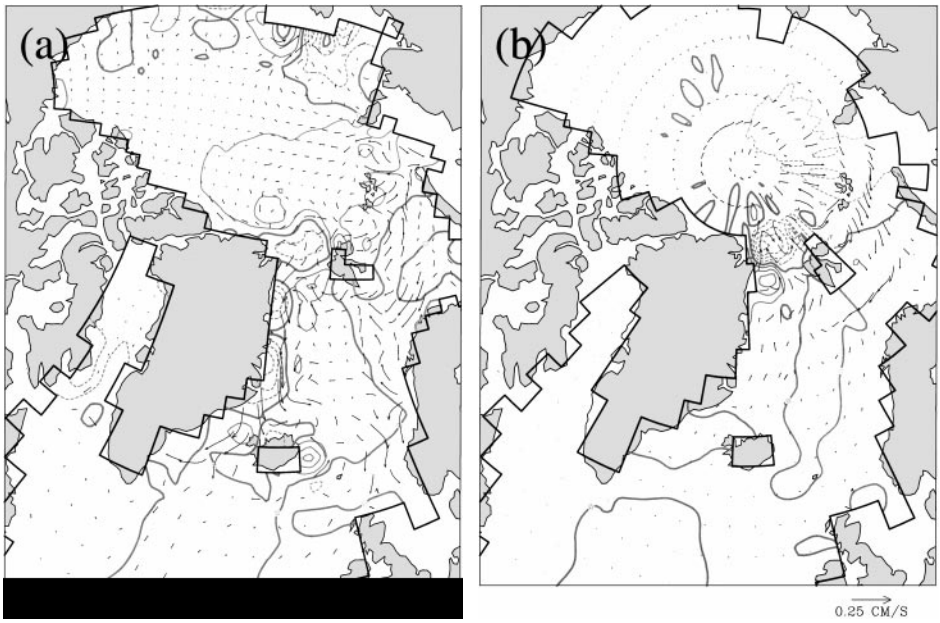

FIG. 6. Velocity and potential density differences for (a) embedded minus unfiltered spherical model (450-day streamlines, contour interval 0.05 sigma units) and (b) filtered minus unfiltered spherical model (1800-day streamlines, contour interval 0.01 sigma units). Note the difference in scales.

between spherical and curvilinear model solutions when both are run on the same latitude–longitude grid. Also, differences in the order of operations and the way that storage is handled have a small impact on execution time, depending on the computer code, platform, and optimisations. The curvilinear model requires some extra calculations, but their cost is largely offset by the precalculation of many combinations of metric factors as two-dimensional arrays in our model. In unfiltered tests carried out on an NEC SX4 computer with code adapted from MOM1, the curvilinear model took up to $3\frac{1}{2}$% longer with some options.

An important reason for adopting a curvilinear coordinate framework in global models is that it allows one to circumvent numerical problems associated with the presence of the North Pole in the Arctic Ocean; in particular, the effects of small grid spacing on computational time steps. Fourier filtering is the method normally chosen to deal with this, and is used in spite of its negative effects because of the very considerable alleviation of time step constraints (by a factor of 1:16 in these experiments) that it provides, which far outweighs the extra computational time needed for carrying out the filtering calculations. However, in comparison with a curvilinear model, which does not require filtering anyway, a filtered spherical model confers no computational advantage, only the disadvantage of performing these extra calculations. Murray and Reason [40] showed that these could increase execution time per time step by 17% in a global model in some formulations. Compared to this figure, the small differences in computing time due to coding differences between the spherical and curvilinear models referred to above are insignificant. Furthermore, a curvilinear grid can often be designed to cover the world ocean or a particular part of it with a smaller number of grid points if a boundary can be made to encircle a large land mass.

To separate solution differences due to filtering from those specifically due to the use of a latitude–longitude grid, we decided to run both filtered and unfiltered simulations. The

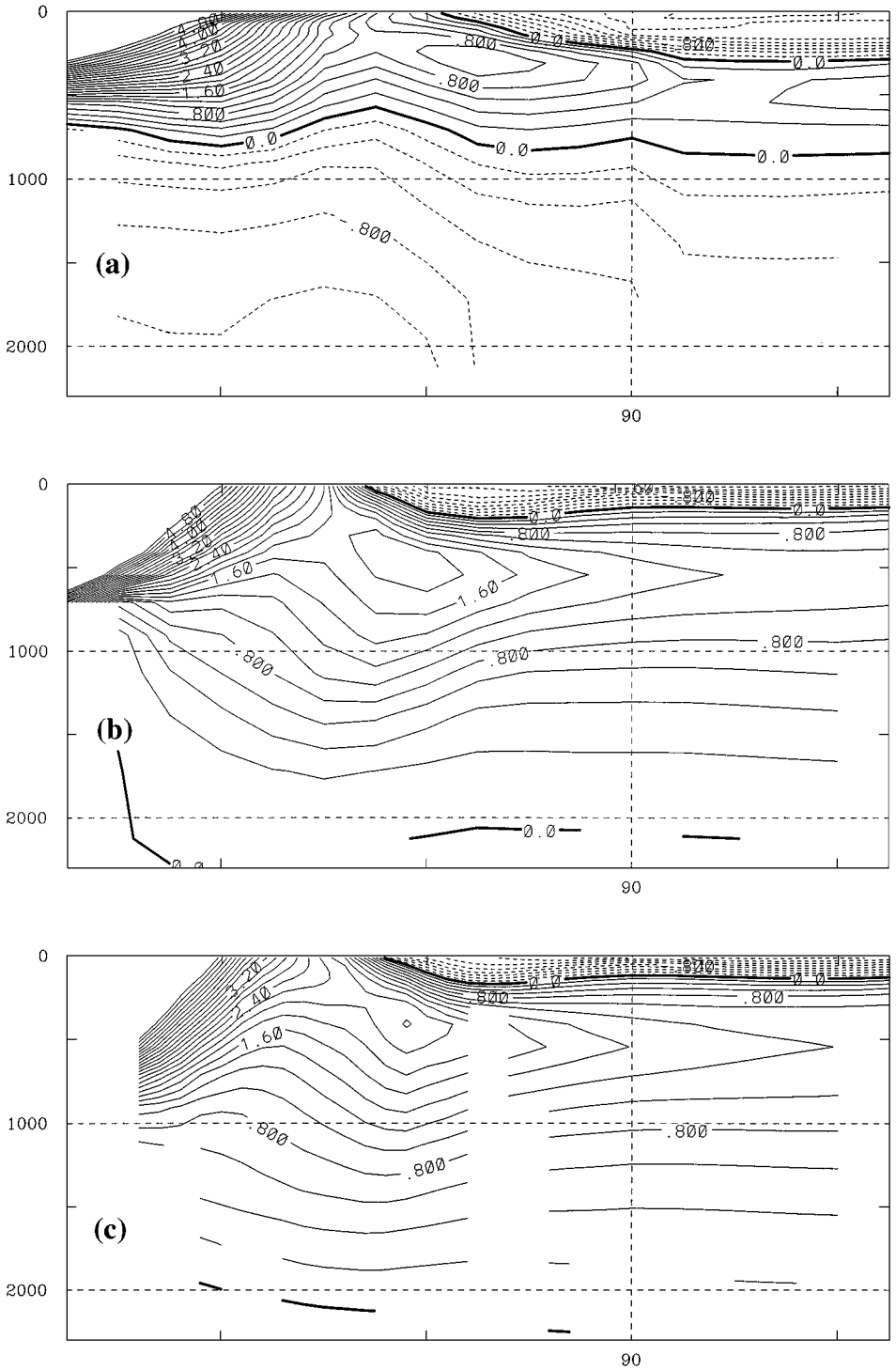

FIG. 7. Potential temperatures along the meridian 2°E–178°W from (a) Levitus and the (b) spherical, (c) bipolar, and (d) embedded grid models (contour interval 0.2°C, dashed contours for subzero temperatures).

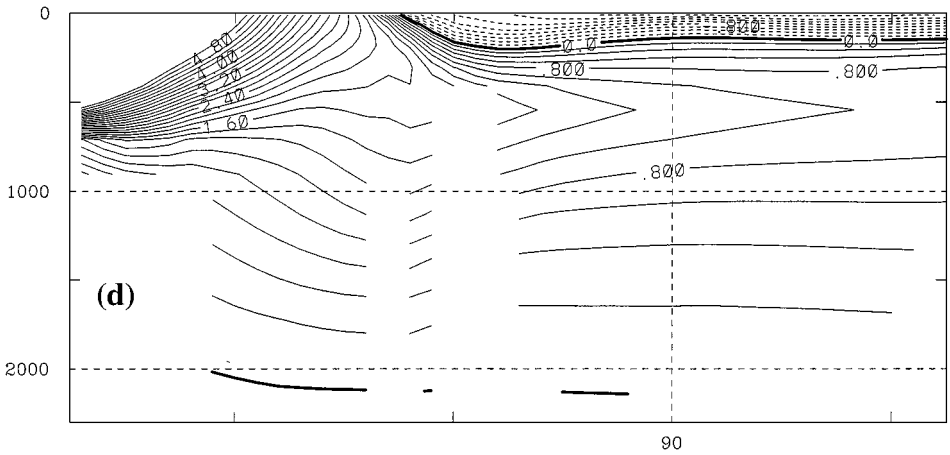

FIG. 7—*Continued*

effects of filtering are more thoroughly dealt with by Murray and Reason [40], mostly using a horizontal mixing formulation; however, a couple of examples are given here from eddy-induced transport experiments (Fig. 4b and Fig. 6b). In these simulations, filtering has had little noticeable effect on plots of the prognostic variables, but some spurious features show in difference plots and in vertical velocity fields. The relative freedom from distortion in the prognostic variables reflects the stabilising effects of using constant restorative forcings, and may not apply to coupled or synoptically forced integrations.

The impact of using various types of curvilinear grid was assessed by comparison with the unfiltered latitude–longitude simulation. As Eby and Holloway [17] recognised, it is not realistic to require an exact correspondence of global simulations with realistic topography because there will always be differences due to interpolation and topography when different grids are used; this is just as true for different latitude–longitude grids—it is not a characteristic of curvilinear grids per se. A reasonable requirement is that different grids should represent the same qualitative features and that there should be a fairly close quantitative agreement in locations remote from topography. Murray and Reason [41], comparing simulations on global grids of varying resolution, found that differences between solutions were very small in midocean provided that similar mixing coefficients were used, but that differences could be large near topography and sometimes noticeable at some distance from important channels, such as the Drake Passage, if differently resolved on different grids. In this connection, the Arctic is challenging for any model comparison because of the dominance of its topography and the complexity of the currents passing through it.

The simulations all showed the major current and water mass features known from observation; however, they did show some deficiencies, and where these were concerned, the correspondence between the models was closer than between models and observations. In the Arctic, the Beaufort Gyre expanded too much into the eastern half of the ocean, and the path of the Transpolar Drift Stream was unrealistically contorted. The upper layers of the eastern Arctic Ocean were insufficiently warm, saline, and dense as a result of the weak inflow through Fram Strait. Because of the absence of a source of high salinity shelf water, the deep water was too warm and insufficiently dense to escape into the Greenland Sea at the bottom levels of Fram Strait. It would be possible to rectify this defect to some extent by employing an interior relaxation or a stronger, preferably

seasonal, surface relaxation over the Siberian shelves or by coupling to an ice model. The most salient deficiency of both latitude–longitude and curvilinear grid arrangements, and the one underlying a number of the deficiencies catalogued above, was the inability of the models to resolve horizontally separated north- and south-directed flows through Fram Strait and, hence, adequately represent the differential advection that takes place through it.

In discussing the realism of the simulations, it should be emphasized that the purpose of the comparison was not to decide upon a suitable simulation for studying the physical oceanography of the Arctic as such, a task more effectively accomplished using a fine resolution ocean or ice–ocean model of just the Arctic; rather, it was to determine what sort of grid arrangement would be most suited to modelling a global ocean in which exchanges with the Arctic Ocean could be well represented while overcoming numerical problems associated with its inclusion. Equilibrium simulations of the type used here provide a quick but only partial answer to this question because the employment of constant restorative forcings tends to suppress climatic feedbacks and remote effects, especially in the Arctic. The full benefit of avoiding filtering and using a well chosen grid arrangement is only likely to be seen when time-varying surface fluxes and coupling with ice and atmosphere are employed; however, such an investigation is outside the scope of this work.

In this study, we have considered the characteristics of integrations carried out on a latitude–longitude grid and on two curvilinear grids which represent two types of singularity placement that work well for representing the Arctic on a global mesh. In addition to removing the north grid pole from the ocean, these two grids have some attractive resolution characteristics in the Arctic region, where they are much needed if Arctic processes are to be adequately represented in a global model. The bipolar grid that we used has very good north–south resolution but poor east–west resolution, even after some compression in the grid meridional direction; this allowed a better representation of the West Greenland and Labrador currents, but provided too little resolution in Fram Strait and other straits. Stronger compression might have overcome this deficiency. The latitude–longitude grid actually gave the best east–west resolution in Fram Strait. Both bipolar and spherical grids suffered from large aspect ratios. The embedded grid seemed to have the best overall arrangement, with fairly isotropic and rather better than global average resolution in the Arctic region; this type of grid also has the advantage of being a latitude–longitude grid over most of the globe and of therefore being amenable to latitudinal compression near the equator or elsewhere if required. All simulations, however, represented the exchanges in Fram Strait similarly, because all used topography in which the strait was artifically widened as necessary to include at least a single line of velocity points. For modelling this particular strait, it is clear that more than one line of velocity points would be desirable.

APPENDIX A

Curvilinear Forms of Differential Operators in Transverse Curvilinear Coordinates

The gradient of a scalar q and the vertical component of the curl of a vector, $\mathbf{V}$, may be written

$$\nabla q = \sum_m \frac{\hat{\mathbf{e}}_m}{h_m} \frac{\partial q}{\partial \xi_m}, \tag{A1}$$

$$\hat{\mathbf{e}}_3 \cdot \boldsymbol{\nabla} \times \mathbf{V} = (\boldsymbol{\nabla} \times \mathbf{V})_3 = \frac{1}{h_1 h_2}\left(\frac{\partial h_2 V_2}{\partial \xi_1} - \frac{\partial h_1 V_1}{\partial \xi_2}\right). \tag{A2}$$

The best expansion of the divergence operator depends on the nature of its argument. For transverse curvilinear coordinates, in which

$$\frac{\partial h_1}{\partial \xi_3} = \frac{\partial h_2}{\partial \xi_3} = \frac{\partial h_3}{\partial \xi_1} = \frac{\partial h_3}{\partial \xi_2} = 0, \tag{A3}$$

the divergence of a vector $\mathbf{V}$, of the product of a tensor A and the gradient of a scalar q, and of a tensor A are given by

$$\boldsymbol{\nabla} \cdot \mathbf{V} = \frac{1}{h_1 h_2}\left[\frac{\partial}{\partial \xi_1}(h_2 V_1) + \frac{\partial}{\partial \xi_2}(h_1 V_2)\right] + \frac{1}{h_3}\frac{\partial V_3}{\partial \xi_3}, \tag{A4}$$

$$\begin{aligned}\boldsymbol{\nabla} \cdot (\mathsf{A}\boldsymbol{\nabla} q) = {} & \frac{1}{h_1 h_2}\left[\frac{\partial}{\partial \xi_1}\left(h_2 \sum_{m=1,3} \frac{A_{1m}}{h_m}\frac{\partial q}{\partial \xi_m}\right) + \frac{\partial}{\partial \xi_2}\left(h_1 \sum_{m=1,3} \frac{A_{2m}}{h_m}\frac{\partial q}{\partial \xi_m}\right)\right] \\ & + \frac{1}{h_3}\frac{\partial}{\partial \xi_3}\left(\sum_{m=1,3} \frac{A_{3m}}{h_m}\frac{\partial q}{\partial \xi_m}\right),\end{aligned} \tag{A5}$$

$$\begin{aligned}\boldsymbol{\nabla} \cdot \mathsf{A} = {} & \left\{\frac{1}{h_1 h_2}\left[\frac{\partial}{\partial \xi_1}(h_2 A_{11}) + \frac{\partial}{\partial \xi_2}(h_1 A_{21}) + A_{21}\frac{\partial h_1}{\partial \xi_2} - A_{22}\frac{\partial h_2}{\partial \xi_1}\right] + \frac{1}{h_3}\frac{\partial}{\partial \xi_3}(A_{31})\right\}\hat{\mathbf{e}}_1 \\ & + \left\{\frac{1}{h_1 h_2}\left[\frac{\partial}{\partial \xi_1}(h_2 A_{12}) + \frac{\partial}{\partial \xi_2}(h_1 A_{22}) + A_{12}\frac{\partial h_2}{\partial \xi_1} - A_{11}\frac{\partial h_1}{\partial \xi_2}\right] + \frac{1}{h_3}\frac{\partial}{\partial \xi_3}(A_{32})\right\}\hat{\mathbf{e}}_2 \\ & + \left\{\frac{1}{h_1 h_2}\left[\frac{\partial}{\partial \xi_1}(h_2 A_{13}) + \frac{\partial}{\partial \xi_2}(h_1 A_{23})\right] + \frac{1}{h_3}\frac{\partial}{\partial \xi_3}(A_{33})\right\}\hat{\mathbf{e}}_3.\end{aligned} \tag{A6}$$

APPENDIX B

Derivation of the Momentum Diffusion Form of the Friction Term

Expanding the expression for $(F_{\mathrm{H}})_1$ in Eq. (23),

$$\begin{aligned}(F_{\mathrm{H}})_1 = {} & \frac{1}{h_1 h_2}\left\{\frac{1}{h_2}\frac{\partial}{\partial \xi_1}\left[\frac{A_M h_2^2}{h_1}\frac{\partial u_1}{\partial \xi_1} - \frac{A_M h_2}{h_1}\frac{\partial h_2}{\partial \xi_1}u_1 - A_M h_2 \frac{\partial u_2}{\partial \xi_2} + \frac{A_M h_2}{h_1}\frac{\partial h_1}{\partial \xi_2}u_2\right]\right. \\ & \left. + \frac{1}{h_1}\frac{\partial}{\partial \xi_2}\left[A_M h_1 \frac{\partial u_2}{\partial \xi_1} - \frac{A_M h_1}{h_2}\frac{\partial h_2}{\partial \xi_1}u_2 + \frac{A_M h_1^2}{h_2}\frac{\partial u_1}{\partial \xi_2} - \frac{A_M h_1}{h_2}\frac{\partial h_1}{\partial \xi_2}u_1\right]\right\} \\ = {} & \frac{1}{h_1 h_2}\left\{\frac{\partial}{\partial \xi_1}\left(A_M \frac{h_2}{h_1}\frac{\partial u_1}{\partial \xi_1}\right) + \frac{A_M}{h_1}\frac{\partial h_2}{\partial \xi_1}\frac{\partial u_1}{\partial \xi_1} - \frac{A_M}{h_1}\frac{\partial h_2}{\partial \xi_1}\frac{\partial u_1}{\partial \xi_1}\right. \\ & - \frac{1}{h_2}\frac{\partial}{\partial \xi_1}\left(A_M \frac{h_2}{h_1}\frac{\partial h_2}{\partial \xi_1}\right)u_1 - A_M \frac{\partial^2 u_2}{\partial \xi_1 \partial \xi_2} - \frac{\partial A_M}{\partial \xi_1}\frac{\partial u_2}{\partial \xi_2} - \frac{A_M}{h_2}\frac{\partial h_2}{\partial \xi_1}\frac{\partial u_2}{\partial \xi_2} \\ & + \frac{A_M}{h_1}\frac{\partial h_1}{\partial \xi_2}\frac{\partial u_2}{\partial \xi_1} + \frac{1}{h_2}\frac{\partial}{\partial \xi_1}\left(A_M \frac{h_2}{h_1}\frac{\partial h_1}{\partial \xi_2}\right)u_2 + A_M \frac{\partial^2 u_2}{\partial \xi_2 \partial \xi_1} + \frac{\partial A_M}{\partial \xi_2}\frac{\partial u_2}{\partial \xi_1} \\ & + \frac{A_M}{h_1}\frac{\partial h_1}{\partial \xi_2}\frac{\partial u_2}{\partial \xi_1} - \frac{A_M}{h_2}\frac{\partial h_2}{\partial \xi_1}\frac{\partial u_2}{\partial \xi_2} - \frac{1}{h_1}\frac{\partial}{\partial \xi_2}\left(A_M \frac{h_1}{h_2}\frac{\partial h_2}{\partial \xi_1}\right)u_2 + \frac{\partial}{\partial \xi_2}\left(A_M \frac{h_1}{h_2}\frac{\partial u_1}{\partial \xi_2}\right) \\ & \left. + \frac{A_M}{h_2}\frac{\partial h_1}{\partial \xi_2}\frac{\partial u_1}{\partial \xi_2} - \frac{A_M}{h_2}\frac{\partial h_1}{\partial \xi_2}\frac{\partial u_1}{\partial \xi_2} - \frac{1}{h_1}\frac{\partial}{\partial \xi_2}\left(A_M \frac{h_1}{h_2}\frac{\partial h_1}{\partial \xi_2}\right)u_1\right\}.\end{aligned}$$

After grouping, cancelling, and rearranging terms, the expression may be written

$$
\begin{aligned}
(F_{\mathrm{H}})_1 = \frac{1}{h_1 h_2}\Bigg\{ & \frac{\partial}{\partial \xi_1}\left(A_M \frac{h_2}{h_1}\frac{\partial u_1}{\partial \xi_1}\right) + \frac{\partial}{\partial \xi_2}\left(A_M \frac{h_1}{h_2}\frac{\partial u_1}{\partial \xi_2}\right) \\
& + \left[\frac{2A_M}{h_1}\frac{\partial h_1}{\partial \xi_2} + \frac{\partial A_M}{\partial \xi_2}\right]\frac{\partial u_2}{\partial \xi_1} - \left[\frac{2A_M}{h_2}\frac{\partial h_2}{\partial \xi_1} + \frac{\partial A_M}{\partial \xi_1}\right]\frac{\partial u_2}{\partial \xi_2} \\
& + \left[-\frac{1}{h_2}\frac{\partial}{\partial \xi_1}\left(A_M \frac{h_2}{h_1}\frac{\partial h_2}{\partial \xi_1}\right) - \frac{1}{h_1}\frac{\partial}{\partial \xi_2}\left(A_M \frac{h_1}{h_2}\frac{\partial h_1}{\partial \xi_2}\right)\right] u_1 \\
& + \left[+\frac{1}{h_2}\frac{\partial}{\partial \xi_1}\left(A_M \frac{h_2}{h_1}\frac{\partial h_1}{\partial \xi_2}\right) - \frac{1}{h_1}\frac{\partial}{\partial \xi_2}\left(A_M \frac{h_1}{h_2}\frac{\partial h_2}{\partial \xi_1}\right)\right] u_2 \Bigg\}.
\end{aligned}
$$

By a similar process, or by symmetry, the ξ_2 term may be shown to be

$$
\begin{aligned}
(F_{\mathrm{H}})_2 = \frac{1}{h_1 h_2}\Bigg\{ & \frac{\partial}{\partial \xi_1}\left(A_M \frac{h_2}{h_1}\frac{\partial u_2}{\partial \xi_1}\right) + \frac{\partial}{\partial \xi_2}\left(A_M \frac{h_1}{h_2}\frac{\partial u_2}{\partial \xi_2}\right) \\
& - \left[\frac{2A_M}{h_1}\frac{\partial h_1}{\partial \xi_2} + \frac{\partial A_M}{\partial \xi_2}\right]\frac{\partial u_1}{\partial \xi_1} + \left[\frac{2A_M}{h_2}\frac{\partial h_2}{\partial \xi_1} + \frac{\partial A_M}{\partial \xi_1}\right]\frac{\partial u_1}{\partial \xi_2} \\
& + \left[-\frac{1}{h_2}\frac{\partial}{\partial \xi_1}\left(A_M \frac{h_2}{h_1}\frac{\partial h_2}{\partial \xi_1}\right) - \frac{1}{h_1}\frac{\partial}{\partial \xi_2}\left(A_M \frac{h_1}{h_2}\frac{\partial h_1}{\partial \xi_2}\right)\right] u_2 \\
& - \left[+\frac{1}{h_2}\frac{\partial}{\partial \xi_1}\left(A_M \frac{h_2}{h_1}\frac{\partial h_1}{\partial \xi_2}\right) - \frac{1}{h_1}\frac{\partial}{\partial \xi_2}\left(A_M \frac{h_1}{h_2}\frac{\partial h_2}{\partial \xi_1}\right)\right] u_1 \Bigg\}.
\end{aligned}
$$

Considering the coefficients, the above equations may be simplified to the forms given in Eq. (24).

APPENDIX C

Grid Spacing and Orientation

Grid generation programs provide a file containing the longitudes and latitudes of points on the four subgrids of the grid array. Topography, forcings, and initial conditions are interpolated to these points in the same way as for a latitude–longitude model. Wind stresses, in addition to interpolation, require rotation to components parallel to the grid axes, and hence a knowledge of their *orientation* at velocity points.

Calculation of derivatives in the model equations also requires a knowledge of grid *spacing*. Although prognostic quantities and other quantities calculated from them are only defined on particular subgrids, the metric coefficients are required on all four subgrids; and it is more economic to precalculate and store them independently than to average them in the model calculations. Here it is assumed that the metric factors are defined in a finite difference sense in terms of distances x and y measured along ξ- or η-directed coordinate lines. For instance, the length of the northern boundary of the (i, j) t-grid cell, which passes through points $(i - \frac{1}{2}, j + \frac{1}{2})$, $(i, j + \frac{1}{2})$, and $(i + \frac{1}{2}, j + \frac{1}{2})$ (see Fig. 1), would be

$$
(h_1)_{i,j+\frac{1}{2}} = (\delta_\xi x)_{i,j+\frac{1}{2}} = x_{i+\frac{1}{2},j+\frac{1}{2}} - x_{i-\frac{1}{2},j+\frac{1}{2}}.
$$

It is not always convenient or possible to calculate grid spacings and orientations analytically; however, because these properties are normally designed to vary smoothly

across the grid, they can be fairly accurately approximated by those of the small circle arc which fits three adjacent (half-integral) points along an x or y coordinate line, as in the example given above.

For many purposes, it is necessary to reinterpolate model output to a latitude–longitude grid. This is not so straightforward as interpolating to the curvilinear grid because the curvilinear coordinates of latitude–longitude points are not known and an analytical inversion of the grid-generation algorithm is not always available. The method that we have used is to search for the nearest curvilinear point to each required latitude–longitude point and then determine the fractional position of the latter in curvilinear grid units, i.e., ξ and η. This calculation is another that requires a knowledge of grid orientations and spacings, and from it is constructed an inverse grid file, which can be efficiently used any number of times for interpolating from a particular curvilinear grid to a particular latitude–longitude grid (or conceivably another curvilinear grid).

APPENDIX D

Reentrant Boundary Conditions

Global models normally have a simple periodic boundary condition,

$$q_{i,j} = q_{i \pm n_i, j},$$

where n_i is the periodicity of the grid in the east–west direction. This is applied by including a repeated longitude column at the east and west boundaries. The northern and southern boundaries are normally closed by land in latitude–longitude models, usually by Antarctica in the south and by a polar island or reclaimed Arctic land mass in the north; however, artificial reentrant northern (or southern) boundary conditions are possible, such as cyclic north–south periodicity or reflection symmetry at some northern latitude (the 'symmetry' option in the GFDL model). A point inversion symmetry is the natural boundary condition for continuity across the pole, but in practice, continuity is achieved using a special computation for a composite polar cell, as mentioned in the Introduction.

In curvilinear models, singularities are normally placed over continents so that the need to give special consideration to the pole is avoided. Bipolar curvilinear grids have just an 'east–west' periodicity, but grids with more than two singularities may require more complicated reentrant conditions. The conic section and embedded rotated grids of Murray [38] have three singularities and may be mapped onto a single rectangular array with three reentrant boundaries: the periodic east and west boundaries, and a northern boundary defined by an arc which joins the two northern singularities and across which the grid meridians pass. From the indices given in Fig. 8 the continuity condition may be expressed as

$$q_{i,j} = q_{\pm n_i/2 + 2i_{\mathrm{sym}} - i,\, 2j_{\mathrm{pole}} - j},$$

where i_{sym} is the (integral or half-integral) index of the symmetry meridian and j_{pole} is the (integral or half-integral) index of the northern grid parallel. In the model as we have used it, the transpolar arc has been a prognostic u-grid row (j_{pole} half-integral), and one repeated t-grid row and one repeated u-grid row beyond the polar arc have been included to enable the computation of derivatives of quantities in the penultimate rows.

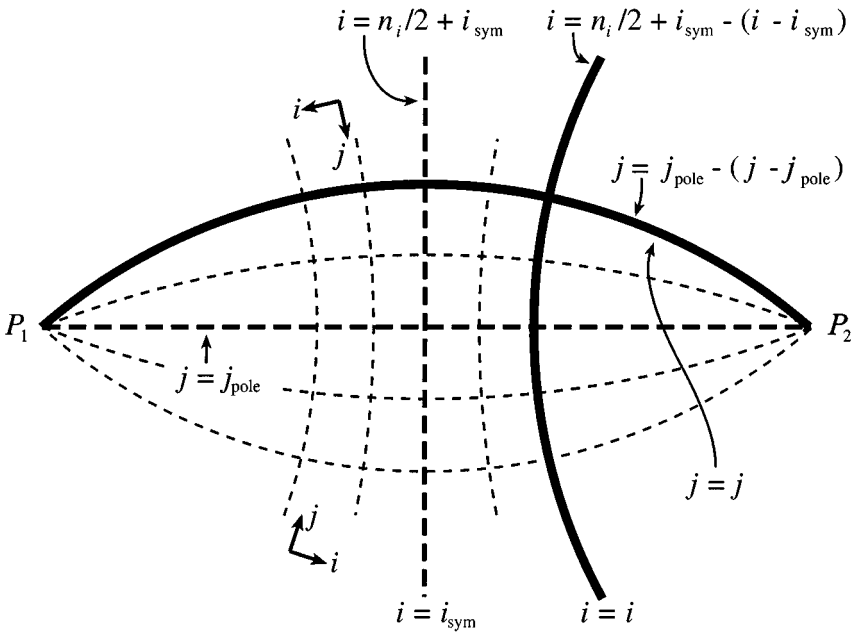

FIG. 8. Scheme of grid lines and indices near the northern array boundary of an embedded rotated or conic section grid. The symmetry meridian and the bounding grid parallel (joining the singularities P_1 and P_2) are shown as bold dashed lines. Representative coordinate axes and indices are shown as seen from below and above the boundary.

APPENDIX E

Integral Relations

In order to prevent nonlinear instabilities and cumulative errors, the finite differencing scheme of Bryan [6] has been designed to conserve certain first and second moment quantities. Semtner [53] has shown that the nondissipative terms conserve global integrals of tracer, tracer variance, and energy in the spherical coordinate model. Following his approach, it is shown here that these integral constraints are also obeyed in the orthogonal curvilinear model.

The time rate of change of the volume integral of tracer due to advection is

$$\sum_{m=1}^{N} \alpha_m \frac{\delta q_m}{\delta t} = -\sum_{m=1}^{N} \sum_{i=1}^{6} A_m^i \, V_m^i \bar{q}_m^i,$$

where α_m is the volume of cell m, q_m is its tracer value, and $\bar{q}_m^i$, A_m^i, V_m^i are the tracer value, area, and exit normal velocity on the ith face. This integral is 0 because V_m^i is 0 on ocean boundaries and antisymmetric with respect to adjacent cells. The result places no restrictions on the way that $\bar{q}_m^i$, A_m^i, or V_m^i are calculated nor does it require that the α_m and V_m^i be calculated consistently; it is thus equally applicable to curvilinear grids. The quantity actually conserved is $\sum_{m=1}^{N} \alpha_m q_m/\delta t$, which allows for a possible variation of time step i.e., δt_m) across the array. The volume integral of the tracer variance, $\sum_{m=1}^{N} \alpha_m q_m^2/\delta t$, is also conserved provided that $\bar{q}_m^i = (q_m + q_m^i)/2$, where q_m^i is the value in the cell sharing

the ith face, since

$$\sum_{m=1}^{N}\alpha_m\frac{\delta q_m^2}{\delta t}=\sum_{m=1}^{N}\alpha_m 2q_m\frac{\delta q_m}{\delta t}=-\sum_{m=1}^{N}\sum_{i=1}^{6}2A_m^iV_m^iq_m\overline{q_m}^i$$
$$=-\sum_{m=1}^{N}q_m^2\sum_{i=1}^{6}A_m^iV_m^i-\sum_{m=1}^{N}\sum_{i=1}^{6}A_m^iV_m^iq_mq_m^i=0. \tag{E1}$$

The first term of the expansion is 0 by continuity. The second term is 0 because $q_mq_m^i$ is symmetric and V_m^i is antisymmetric for pairs of adjacent cells, and because $V_m^i=0$ on boundaries. Once again, there is nothing that restricts this conclusion to a particular coordinate system. The familiar treatment reproduced above makes the implied approximation that errors due to the time discretisation are negligible, i.e., that

$$\left(\delta_{2t}q_m^2\right)^{(n)}=\left(q_m^{(n+1)}+q_m^{(n-1)}\right)\left(q_m^{(n+1)}-q_m^{(n-1)}\right)=2\left(\overline{q_m}^{2t}\right)^{(n)}\delta q_m^{(n)}\approx 2q_m^{(n)}\delta q_m^{(n)}.$$

This approximation requires that measures be taken to stabilise and suppress the computational mode in time which may be present in the leapfrog scheme.

In the momentum equations, there are two terms which should conserve variance, that is to say kinetic energy—the advective term and the Coriolis force term. The advective term for each component contains an elliptical or 'flux-form' part and a metric part. The former conserves variance for reasons similar to those in the case of scalar variables except that, as Semtner pointed out, a no-slip condition ($\mathbf{u}_m^i=0$) is necessary to make the cross term (in the expansion of Eq. E1) zero, since V_m^i may be nonzero. The metric terms for the two components also conserve variance, but only in combination. From Eqs. (33) and (34),

$$\sum_{m=1}^{N}\alpha_m\frac{\delta\left(u_m^2+v_m^2\right)}{\delta t}=-\sum_{m=1}^{N}\sum_{i=1}^{6}2A_m^iV_m^i\left[u_m^i\overline{u}_m^i+v_m^i\overline{v}_m^i\right]$$
$$+\sum_{m=1}^{N}2\alpha_m\{u_m[-(L_1u_m-L_2v_m)v_m]+v_m[(L_1u_m-L_2v_m)u_m]\}=0.$$

The work done by (the explicit part of) the Coriolis term, $u_m\cdot fv_m+v_m\cdot(-fu_m)$, is also zero when both components are included, and this applies at every point.

Work may be done by hydrostatic pressure gradient forces when they are not geostrophically balanced. Semtner [53] showed that this is equal to the work done by buoyancy forces, i.e., to the potential energy loss, so that total energy is conserved in this process. In the curvilinear case, the work done by the pressure gradient forces is

$$-\frac{1}{\rho_0}\sum_{m=1}^{N}(h_1h_2)_{uu}(h_3)_t\left[u_{uu}\,\delta_\xi\overline{p_{ttt}}^{\eta}/(h_1)_{uu}+v_{uu}\,\delta_\eta\overline{p_{ttt}}^{\xi}/(h_2)_{uu}\right]$$
$$=-\frac{1}{\rho_0}\sum_{m=1}^{N}(h_3)_t\left[(uh_2)_{uu}\,\delta_\xi\overline{p_{ttt}}^{\eta}+(vh_1)_{uu}\,\delta_\eta\overline{p_{ttt}}^{\xi}\right]$$
$$=-\frac{1}{\rho_0}\sum_{m=1}^{N}(h_3)_t\left[\delta_\xi\overline{(uh_2)_{uu}}^{\eta}+\delta_\eta\overline{(vh_1)_{uu}}^{\xi}\right]p_{ttt}.$$

The second step results from a rearrangement of the expanded terms around p, which is possible since normal velocities across ocean boundaries are zero (*vide* [43]). On applying the hydrostatic relation and rearranging terms around w, the work done by buoyancy forces may be written

$$-\frac{g}{\rho_0}\sum_{m=1}^{N}(h_1h_2)_{tt}\,w_{ttw}\,\overline{\rho_{ttt}(h_3)_t}^{\zeta}=\frac{1}{\rho_0}\sum_{m=1}^{N}(h_1h_2)_{tt}\,w_{ttw}\,\delta_\zeta\,p_{ttt}=\frac{1}{\rho_0}\sum_{m=1}^{N}(h_1h_2)_{tt}\,\delta_\zeta\,w_{ttw}\,p_{ttt}.$$

The two quantities are equal provided that

$$(h_1h_2)_{tt}\,\delta_\zeta\,w_{ttw}=-(h_3)_t\left[\delta_\xi\overline{(uh_2)_{uu}}^{\eta}+\delta_\eta\overline{(vh_1)_{uu}}^{\xi}\right].$$

This will be recognised as a form of the continuity equation. As in the spherical model, the discretisation requires the horizontal mass fluxes at t-cell faces to be represented as weighted averages.

Eddy-induced transport conserves tracers and tracer variance when parameterised as a Gent–McWilliams advection, since no restrictions are placed on the interfacial velocities in Eq. (E1) except that normal velocities must be zero at boundaries. It thus conserves heat energy; however, it is not designed to conserve mechanical energy, but rather to dissipate it in a manner characteristic of the breakdown of baroclinic instability: there is thus no need for eddy-induced velocities to be weighted in any special way, and it is convenient to use values calculated at cell interfaces, as has been done in Eq. (32). Skew diffusion also conserves tracers, but its variance-conserving properties depend upon the numerics used for the rotated diffusion tensor. Griffies [24] shows that skew diffusion conserves variance when formulated using the Griffies *et al.* [25] numerics. When implemented using Cox [13] numerics, skew diffusion does not conserve tracer variance; however, it can reduce or eliminate (in the case of $A_E = A_I$) the *anti*diffusive tendency of the isopycnal diffusion part of the K_{13} and K_{23} terms. This has the practical benefit of helping to suppress checkerboard waves in the tracer fields, which may be excited by dispersion or instability in the Cox isopycnal scheme: the Gent–McWilliams parameterisation is unable to do this since it is a component of centred advection, which has no effect on waves at the grid scale.

ACKNOWLEDGMENT

Funding from the Antarctic Science Advisory Committee administered by the Australian Antarctic Division of the Department of the Environment, Sport, and Territories is gratefully acknowledged.

REFERENCES

1. K. Aagaard, E. Fahrbach, J. Meincke, and J. H. Swift, *J. Geophys. Res.* **96**, 20,433 (1991).
2. K. Aagaard, A. Foldvik, and S. R. Hillman, *J. Geophys. Res.* **92**, 3778 (1987).
3. K. Aagaard, J. H. Swift, and E. C. Carmack, *J. Geophys. Res.* **90**, 4833 (1985).
4. G. K. Batchelor, *An Introduction to Fluid Dynamics* (Cambridge Univ. Press, Cambridge, U.K., 1967).
5. A. F. Blumberg and G. L. Mellor, A description of a three-dimensional coastal ocean circulation model, in *Three-Dimensional Coastal Ocean Models, Coastal Estuarine Science, Vol. 4*, edited by N. Heaps (Am. Geophys. Union, Washington, DC, 1987), p. 1.
6. K. Bryan, *J. Comput. Phys.* **4**, 347 (1969).

7. K. Bryan, *J. Phys. Oceanogr.* **14**, 666 (1984).
8. K. Bryan, The design of numerical models of the ocean circulation, in *Oceanic Circulation Models: Combining Data and Dynamics*, edited by D. L. T. Anderson and J. Willebrand (Kluwer Academic, Dordrecht/Norwell, MA, 1989), p. 465.
9. K. Bryan and M. D. Cox, *Tellus* **19**, 54 (1967).
10. R. Colony and A. S. Thorndike, *J. Geophys. Res.* **89**, 10,623 (1984).
11. A. C. Coward, P. D. Killworth, and J. R. Blundell, *J. Geophys. Res.* **99**, 22,725 (1994).
12. M. D. Cox, *A Primitive Equation, 3-dimensional Model of the Ocean*, Ocean Group Technical Report No. 1 (Geophys. Fluid Dyn. Lab. Princeton, NJ, 1984).
13. M. D. Cox, *Ocean Modelling* **74**, 1 (1987).
14. G. Danabasoglu and J. C. McWilliams, *J. Climate* **8**, 2967 (1995).
15. E. Deleersnijder, J.-P. Van Ypersele, and J.-M. Campin, *Ocean Modelling* **100**, 7 (1993).
16. G. Dietrich, K. Kalle, W. Krauss, and G. Siedler, *General Oceanography, An Introduction*, 2nd ed. (Wiley, New York, 1980).
17. M. Eby and G. Holloway, *Climate Dyn.* **10**, 241 (1994).
18. T. Ezer and G. L. Mellor, *J. Geophys. Res.* **99**, 14,159 (1994).
19. P. R. Gent and J. C. McWilliams, *J. Phys. Oceanogr* **20**, 150 (1990).
20. P. R. Gent, J. Willebrand, T. J. McDougall, and J. C. McWilliams, *J. Phys. Oceanogr.* **25**, 463 (1995).
21. R. Gerdes, *J. Geophys. Res.* **98**, 14,683 (1993).
22. R. Gerdes, C. Köberle, and J. Willebrand, *Climate Dyn.* **5**, 211 (1991).
23. A. E. Green and W. Zerna, *Theoretical Elasticity* (Oxford Univ. Press, London, 1954).
24. S. M. Griffies, *J. Phys. Oceanogr.* **28**, 831 (1998).
25. S. M. Griffies, A. Gnanadesikan, R. C. Pacanowski, V. D. Larichev, J. K. Dukowicz, and R. D. Smith, *J. Phys. Oceanogr.* **28**, 805 (1998).
26. S. M. Griffies and R. W. Hallberg, *Mon. Wea. Rev.* **128**, 2935 (2000).
27. D. B. Haidvogel, J. L. Wilkin, and R. Young, *J. Comput. Phys.* **94**, 151 (1991).
28. S. Häkkinen and G. L. Mellor, *J. Geophys. Res.* **97**, 20,285 (1992).
29. S. Hellerman and M. Rosenstein, *J. Phys. Oceanogr.* **13**, 1093 (1983).
30. D. C. Ives and R. M. Zacharias, Conformal mapping and orthogonal grid generation, presented at AIAA/SAE/ASME/ASEE 23rd Joint Propulsion Conference, San Diego, 1987.
31. A. D. J. Kirwan, *J. Geophys. Res.* **74**, 6953 (1969).
32. E. B. Kraus, Diapycnal Mixing, in *Climate-Ocean Interaction*, edited by M. E. Schlesinger (Kluwer Academic, Dordrecht/Norwell, MA, 1990), p. 269.
33. S. Levitus, *Climatological Atlas of the World Ocean*, NOAA Prof. Pap. 13 (U.S. Govt. Printing Office, Washington, DC, 1982).
34. G. Madec and M. Imbard, *Climate Dyn.* **12**, 381 (1996).
35. L. E. Malvern, *Introduction to the Mechanics of a Continuous Medium* (Prentice-Hall, Englewood Cliffs, NJ, 1969).
36. O. Marti, G. Madec, and P. Delecleuse, *J. Geophys. Res.* **97**, 12,763 (1992).
37. G. L. Mellor, *User's Guide for a Three-Dimensional, Primitive Equation, Numerical Ocean Model* (Atmospheric and Oceanic Sciences Program, Princeton Univ. Princeton, NJ, 1993).
38. R. J. Murray, *J. Comput. Phys.* **126**, 251 (1996).
39. R. J. Murray and C. J. C. Reason, *J. Phys. Oceanogr.* **29**, 2851 (1999).
40. R. J. Murray and C. J. C. Reason, Fourier filtering and coefficient tapering at the North Pole in OGCMS, *Ocean Modelling*, to appear.
41. R. J. Murray and C. J. C. Reason, A curvilinear ocean model using a grid regionally compressed in the South Indian Ocean, *J. Phys. Oceanogr.*, to appear.
42. NCAR Oceanography Section, *The NCAR CSM Ocean Model*, NCAR Tech. Note NCAR/TN-423 + STR (1996).

43. R. C. Pacanowski, *MOM 2 Documentation, User's Guide, and Reference Manual*, Ocean Group Tech. Report No. 3, Geophys. Fluid Dyn. Lab. Princeton, NJ (1995).
44. R. C. Pacanowski and S. M. Griffies, *MOM 3.0 Manual* (NOAA/Geophysical Fluid Dynamics Laboratory, Princeton, NJ, 1999).
45. R. C. Pacanowski, K. Dixon, and A. Rosati, *The GFDL Modular Ocean Model User Guide*, Ocean Group Tech. Report No. 2, Geophy. Fluid Dyn. Lab. Princeton, NJ (1991).
46. C. L. Parkinson, J. C. Comiso, H. J. Zwally, D. J. Cavalieri, P. Gloersen, and W. J. Campbell, *Arctic Sea Ice, 1973-1976: Satellite Passive-Microwave Observations*, NASA Spec. Publ. SP-489 (1987).
47. N. A. Phillips, *J. Atmos. Sci.* **23**, 626 (1966).
48. D. Quadfasel, J.-C. Gascard, and K.-P. Koltermann, *J. Geophys. Res.* **92**, 6719 (1987).
49. M. H. Redi, *J. Phys. Oceanogr.* **12**, 1154 (1982).
50. R. D. Richtmyer and K. W. Morton, *Difference Methods for Initial Value Problems*, 2nd ed. (Wiley–Interscience, New York, 1967).
51. A. Rosati and K. Miyakoda, *J. Phys. Oceanogr.* **18**, 1601 (1988).
52. A. J. Semtner, Jr., *An Oceanic General Circulation Model with Bottom Topography, Numerical Simulation of Weather and Climate*, Tech. Report No. 9, Univ. of California, Los Angeles (1974).
53. A. J. Semtner, Jr., Finite-difference formulation of a world ocean model, in *Advanced Physical Oceanographic Numerical Modelling*, edited by J. J. O'Brien (Reidel, Dordrecht, 1986), p. 187.
54. J. Smagorinsky, *Mon. Wea. Rev.* **91**, 99 (1963).
55. J. Smagorinsky, Some historical remarks on the use of nonlinear viscosities, in *Large Eddy Simulation of Complex Engineering and Geophysical Flows*, edited by B. Galerpin and S. A. Orszag (Cambridge Univ. Press, Cambridge, UK, 1993), p. 4.
56. W. M. Smethie, Jr., D. W. Chipman, J. H. Swift, and K. P. Koltermann, *Deep-Sea Res.* **35**, 347 (1988).
57. R. D. Smith, S. Kortas, and B. Meltz, *Curvilinear Coordinates for Global Ocean Models*, Tech. Note LA-UR-95-1146, Los Alamos Natl. Lab., Los Alamos, NM (1995), unpublished.
58. J. H. Swift, T. Takahashi, and H. D. Livingston, *J. Geophys. Res.* **88**, 5981 (1983).
59. M. Tomczak and J. S. Godfrey, *Regional Oceanography: An Introduction* (Pergamon, Elmsford, NY, 1994).
60. M. R. Wadley and G. R. Bigg, *Ocean Modelling* **1**, 71 (2000).
61. R. C. Wajsowicz, *J. Phys. Oceanogr.* **16**, 773 (1986).
62. R. C. Wajsowicz, *J. Comput. Phys.* **105**, 333 (1993).
63. D. J. Webb, B. A. de Cuevas, and A. C. Coward, *The First Main Run of the OCCAM Global Ocean Model*, Internal Document No. 34, Southampton Oceanography Centre (1998).
64. M. E. Wickett, P. B. Duffy, and G. Rodrigue, *Ocean Modelling* **2**, 85 (2000).
65. J. L. Wilkin, *A Computer Program for Generating Two-Dimensional Orthogonal Curvilinear Coordinate Grids* (1987), unpublished.
66. J. L. Wilkin and K. S. Hedström, *User's Manual for an Orthogonal Curvilinear Grid-Generation Package*, http://marine.rutgers.edu/po/index.html (1998).
67. G. P. Williams, *J. Atmos. Sci.* **29**, 870 (1972).